Mikada, H., Moore, G.F., Taira, A., Becker, K., Moore, J.C., and Klaus, A. (Eds.)
Proceedings of the Ocean Drilling Program, Scientific Results Volume 190/196

6. Clay Mineralogy of Mudstones from the Nankai Trough Reference Sites 1173 and 1177 and Frontal Accretionary Prism Site 1174[1]

Joan F. Steurer[2] and Michael B. Underwood[2]

ABSTRACT

X-ray diffraction analyses of the clay-sized fraction of sediments from the Nankai Trough and Shikoku Basin (Sites 1173, 1174, and 1177 of the Ocean Drilling Program) reveal spatial and temporal trends in clay minerals and diagenesis. More detrital smectite was transported into the Shikoku Basin during the early–middle Miocene than what we observe today, and smectite input decreased progressively through the late Miocene and Pliocene. Volcanic ash has been altered to dioctahedral smectite in the upper Shikoku Basin facies at Site 1173; the ash alteration front shifts upsection to the outer trench-wedge facies at Site 1174. At greater depths (lower Shikoku Basin facies), smectite alters to illite/smectite mixed-layer clay, but reaction progress is incomplete. Using ambient geothermal conditions, a kinetic model overpredicts the amount of illite in illite/smectite clays by 15%–20% at Site 1174. Numerical simulations come closer to observations if the concentration of potassium in pore water is reduced or the time of burial is shortened. Model results match X-ray diffraction results fairly well at Site 1173. The geothermal gradient at Site 1177 is substantially lower than at Sites 1173 and 1174; consequently, volcanic ash alters to smectite in lower Shikoku Basin deposits but smectite–illite diagenesis has not started. The absolute abundance of smectite in mudstones from Site 1177 is sufficient (30–60 wt%) to influence the strata's shear strength and hydrogeology as they subduct along the Ashizuri Transect.

[1]Steurer, J.F., and Underwood, M.B., 2003. Clay mineralogy of mudstones from the Nankai Trough reference Sites 1173 and 1177 and frontal accretionary prism Site 1174. *In* Mikada, H., Moore, G.F., Taira, A., Becker, K., Moore, J.C., and Klaus, A. (Eds.), *Proc. ODP, Sci. Results,* 190/196, 1–37 [Online]. Available from World Wide Web: <http://www-odp.tamu.edu/publications/190196SR/VOLUME/CHAPTERS/211.PDF>. [Cited YYYY-MM-DD]
[2]Department of Geological Sciences, University of Missouri, Columbia, 101 Geology Building, Columbia MO 65211, USA. Correspondence author: **underwoodm@missouri.edu**

Initial receipt: 18 November 2002
Acceptance: 5 August 2003
Web publication: 26 November 2003
Ms 190SR-211

INTRODUCTION

The objective of this paper is to document stratigraphic trends in clay mineralogy and clay diagenesis at Sites 1173, 1174, and 1177, which were cored by the Ocean Drilling Program (ODP) in the Nankai Trough (Fig. F1). During studies of marine sedimentation, clay minerals provide important information for determining the detrital origin of sediment (e.g., Hathon and Underwood, 1991; Fagel et al., 1992; Petschick et al., 1996). Detrital chlorite, for example, is a typical product of physical weathering of plutonic and metamorphic rocks, as well as shale; chlorite tends to increase in ocean sediments toward higher latitudes where physical weathering predominates (Biscaye, 1965; Naidu and Mowatt, 1983). Kaolinite is more prevalent in tropical latitudes where chemical weathering is more intense (Biscaye, 1965; Faugeres et al., 1991; Petschick et al., 1996). Detrital illite resists chemical weathering and is common in most continental soils (Biscaye, 1965). Illite and illite/smectite (I/S) mixed-layer clays are common low-temperature diagenetic products in marine basins (Burst, 1969; Perry and Hower, 1970; Hower et al., 1976).

Fagel et al. (2001) showed how subtle differences among minerals belonging to the smectite group could be used to decipher changes in detrital provenance and dispersal route through time. This type of approach is possible because different precursors and weathering processes produce different varieties of smectite. In brief, dioctahedral smectites (beidellite and montmorillonite) are typical products of silicic volcanic sources (Chamley, 1989), although iron montmorillonite can also be produced from biogenic silica (Hein et al., 1979). Hydrothermal alteration of basalt produces dioctahedral nontronite, but nontronite is also found in rocks exposed to greenschist facies metamorphism. Saponite (trioctahedral smectite) and celadonite (dioctahedral silica-rich mica) form during alteration of crystalline basalt and basaltic glass, especially during the early stages of hydrothermal circulation (e.g., Porter et al., 2000). Saponite also results from zeolite facies metamorphism and can be eroded from an island arc. In the late stages of alteration of basaltic glass, saponite evolves to dioctahedral (Mg, Fe^{2+} rich) smectite (Chamley, 1989).

In addition to their value as provenance indicators, clay minerals exert a significant impact on sediment shear strength. Clay-sized material, especially expandable clay minerals, affects both internal friction and permeability (Olson, 1974; Wang, 1980; Shimamoto and Logan, 1981; Morrow et al., 1984; Logan and Rauenzahn, 1987; Freed and Peacor, 1989a; Mitchell, 1993). Liberation of water from smectite's interlayer site shrinks the original mineral volume by as much as 35% if illitization goes to ~80% completion (Bird, 1984; Bruce, 1984; Colten-Bradley, 1987). Dehydration during the illite–smectite reaction may be a source of low-chloride fluids in accretionary prisms (Kastner et al., 1991). The lower permeability of clay-rich sediments can cause pore fluid pressure to increase, thereby reducing effective normal stress (Moore and Vrolijk, 1992). Compressibility also changes with clay content (Robinson and Allam, 1998). It is important, therefore, to document the original composition of sediment and to show how that composition changes as pressure and temperature increase. To help assess the extent of smectite–illite diagenesis in the frontal Nankai subduction zone, we utilized the kinetic model of Huang et al. (1993) to generate numerical simulations. Understanding how sediment composition evolves in three di-

F1. Nankai Trough study area, p. 19.

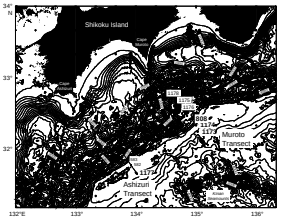

mensions at the Nankai prism toe is an important step in predicting how mechanical behavior changes at greater depths along the subduction boundary.

LITHOSTRATIGRAPHIC CONTEXT

The Nankai Trough and accretionary prism are situated where the Philippine Sea plate (Shikoku Basin) is subducting beneath the Eurasian plate (Moore et al., 2001; Shipboard Scientific Party, 2001b). Drilling during Leg 190 took place along two transects, the eastern Muroto Transect and the western Ashizuri Transect (Fig. F1). Two reference sites were drilled to provide baseline data for characterizing the sediment prior to subduction: Site 1173 (Muroto Transect) and Site 1177 (Ashizuri Transect). Site 1174 penetrated a frontal protothrust and the décollement ~2 km seaward of ODP Site 808 (Fig. F1).

As demonstrated during ODP Leg 131 (Taira et al., 1992; Pickering et al., 1993; Taira and Ashi, 1993), the stratigraphic section entering Nankai Trough from the central part of the Shikoku Basin is more or less consistent with models of accreting margins (e.g., Piper et al., 1973; Dickinson and Seely, 1979) in that it coarsens and thickens upward as the subducting plate approaches land. At Site 1173 (Fig. F2), the base of the Quaternary trench-wedge facies is 102.14 meters below seafloor (mbsf) and the strata consist of hemipelagic mud interbedded with silt, sandy silt, and silty sand turbidites. The upper Shikoku Basin facies (Pliocene–Quaternary; 102.14–445.92 mbsf) was deposited by hemipelagic settling and ash falls. The lower Shikoku Basin facies (Pliocene–middle Miocene; 445.92–790.3 mbsf) is also hemipelagic but lacks recognizable ash layers. The lower Shikoku Basin facies is underlain by a volcaniclastic facies and basalt (Shipboard Scientific Party, 2001c). These same basic facies relations are present at Site 1174 (Fig. F3), but the Quaternary trench-wedge facies extends to 483.23 mbsf, the upper Shikoku Basin facies extends from 483.23 to 660.99 mbsf, and the lower Shikoku Basin facies extends to 1102.45 mbsf (Shipboard Scientific Party, 2001d).

The Ashizuri Transect is located along the distal flanks of the Shikoku Basin spreading center (Fig. F1). Site 1177 (Fig. F4) differs from stratigraphic sections along the Muroto Transect because it does not show a coarsening-upward trend. The trench-wedge facies was not cored, but the upper Shikoku Basin facies (Pliocene) extends from 300.20 to 401.76 mbsf (Shipboard Scientific Party, 2001e). This unit consists of hemipelagic mud and abundant volcanic ash layers. The lower Shikoku Basin hemipelagic facies (lower Pliocene–upper Miocene; 401.76–449.30 mbsf) comprises hemipelagic mudstone and scattered intervals of siliceous claystone. The lower Shikoku Basin turbidite facies (lower–upper Miocene; 449.30–748.35 mbsf) contains abundant siliciclastic sand layers with rare beds of gravel and mudstone-clast conglomerate. A volcaniclastic-rich facies (lower Miocene) extends to 831.08 mbsf and contains variegated mudstone, thin turbidites, and volcanic ash.

Previous studies of detrital clay minerals in the Nankai Trough and Shikoku Basin include those by Cook et al. (1975), Chamley (1980), Chamley et al. (1986), and Underwood et al. (1993a, 1993b). All of those results show a preponderance of detrital illite and chlorite in the Quaternary trench-wedge facies. Details about the illite (e.g., crystallinity index, polytype, and bo lattice dimension) are consistent with their erosion from low-grade metasedimentary rocks, which are widespread

F2. Site 1173 stratigraphic column, p. 20.

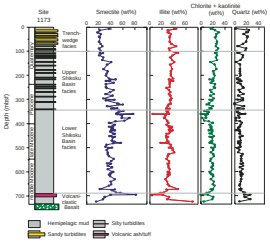

F3. Site 1174 stratigraphic column, p. 21.

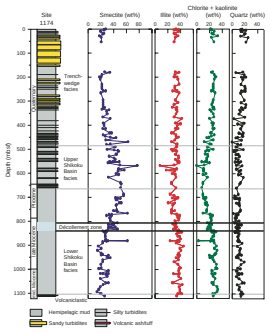

F4. Site 1177 stratigraphic column, p. 22.

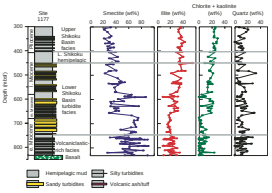

throughout the Outer Zone of Japan (Underwood et al., 1993a). When clay provenance indicators are combined with data from sand petrography and paleoflow indicators (Taira and Niitsuma, 1986; Marsaglia et al., 1992; Pickering et al., 1992; **Fergusson,** this volume), interpretations suggest that the Quaternary trench wedge originated primarily through axial transport from sources located in the Izu-Honshu collision zone of central Japan (Underwood and Pickering, 1996).

In contrast to the Quaternary trench wedge, strata in the Shikoku Basin (Sites 297, 442, 443, and 444 of the Deep Sea Drilling Project) show progressive enrichment of smectite with increasing depth and age (Cook et al., 1975; Chamley, 1980). Previous workers also demonstrated that smectite increases monotonically in the upper Shikoku Basin facies at Site 808, but Underwood et al. (1993b) were not able to discriminate convincingly between the effects of changing detrital sources and/or transport paths through time, as opposed to the effects of in situ ash-to-smectite and smectite–illite diagenesis. Subsequent work by Masuda et al. (1996) showed that glass shards in interbedded volcanic ash layers alter to dioctahedral smectite (aluminum-rich beidellite) and potassium-rich clinoptilolite. The illite–smectite reaction has been inhibited in discrete beds of volcanic ash (Masuda et al., 1996), but there is clear evidence for progressive smectite–illite alteration and uptake of potassium in the bulk mudstones of Shikoku Basin (Underwood et al., 1993b; Underwood and Pickering, 1996; Masuda et al., 2001). Underwood et al. (1993b) speculated that illite–smectite diagenetic progress at Site 808 is a recent response to rapid sedimentary burial beneath the trench wedge (i.e., in the last 0.5 m.y.), but they had no data from an appropriate reference site to constrain the degree of diagenesis seaward of the trench.

LABORATORY METHODS

Sample Preparation

To prepare samples for X-ray diffraction (XRD) analyses, specimens of mud and mudstone were gently crumbled and placed in a glass beaker with 3% H_2O_2 for at least 24 hr until digestion of organic matter stopped. We then added 250 mL of 4 g/L sodium hexametaphosphate to disperse the clays. Further disaggregation was accomplished in an ultrasonic bath. Heavily indurated samples were exposed to additional crushing and repeated ultrasonic dispersal. Samples were then washed via centrifugation (using six 60-mL tubes per sample at 8200 rpm for 25 min), resuspended in 360 mL of deionized distilled water, washed again, and transferred in suspension to a 125-mL plastic bottle. After further dispersion with an ultrasonic cell disruptor, we separated the <2-µm fraction using a centrifuge at 1000 rpm for 2 min, 24 s. Slides were prepared for XRD as oriented aggregates to enhance the clay mineral basal reflections, using the filter-peel method with a 0.45-µm membrane. Slides were solvated in an ethylene glycol atmosphere overnight at 60°C to expand the smectite. The time elapsed between removal from the ethylene glycol chamber and scanning was <80 min to minimize evaporation.

X-Ray Diffraction Analysis

A Scintag PAD V X-ray diffractometer was used to scan slides from 3° to 23°2θ at the following parameters: radiation = CuK_{α}; scan rate = 1°/min; step size = 0.01; voltage = 40 kV; current = 30 mA; and slits = 0.2 mm. Data processing utilized MacDiff software (Petschick, 2001). Profiles were smoothed using the MacDiff standard weighted means 17-term filter. To correct for misalignments of the goniometer and slide holder, we shifted each diffractogram to realign the quartz (100) reflection at 4.26 Å.

Relative Mineral Abundances

To estimate relative abundances of minerals in the clay-sized fraction by weight, we measured the integrated peak areas for basal reflections of smectite, illite, and chlorite, plus quartz. The targeted peaks are shown in Figure F5: smectite (001) at ~17 Å, illite (001) at ~10 Å, chlorite (002) at ~7 Å, and quartz (100) at 4.26 Å. Some difficulty with this method arises from peak overlap. The chlorite (001) peak occurs on the shoulder of the glycol-solvated smectite (001) peak at ~14 Å. More problematic is the complete overlap of chlorite (002) and kaolinite (001) peaks at ~7 Å. Although contents of kaolinite are probably small, we report the 7-Å values as chlorite (+ kaolinite). Interlayers of illite also affect the geometry of the smectite (001) peak, and the I/S (001)/(002) peak merges into the illite (001) peak as the percent illite in I/S increases. This interference adds counts from mixed-layer clay to peak-area values for both smectite and illite.

Another challenge in determining relative mineral abundance in natural sediments is selection of accurate weighting factors. One common method (Biscaye, 1965) multiplies the peak area of smectite (001) by 1×, illite (001) by 4×, and chlorite (002) by 2×, regardless of each mineral's abundance. The peak area generated by a given phase and reflection increases with that mineral's abundance, but each additional phase in a mixture also affects the intensity of all other reflections differently. Thus, to improve the accuracy of bulk powder analysis, Fisher and Underwood (1995) employed singular value decomposition (SVD) to solve for normalization factors using standard mineral mixtures with known weight percentages. Underwood et al. (this volume) solved for SVD weighting factors for the clay-sized fraction using a similar approach; they also completed a thorough analysis of error. We describe herein relative abundances (weight percent) of smectite, illite, chlorite, and quartz as calculated by SVD factors, but we also report the weighted peak areas for smectite, illite, and chlorite using Biscaye (1965) factors to make simplify comparisons with older data sets.

Chlorite and Kaolinite Peak Overlap

Previous workers showed that kaolinite is present in minor amounts at Site 808, ranging from 8% to 20% of the 7-Å peak area (Orr, 1992; see also Chamley et al., 1986). To extend the results of Orr (1992), we selected five representative samples from Sites 1173 and 1177 and boiled them for 2 hr in 1-N HCl. This treatment dissolves chlorite, so a peak remaining at 7 Å indicates the presence of kaolinite (Moore and Reynolds, 1997). Disappearance of the chlorite (003) reflection at 4.77 Å confirms the mineral's removal (Fig. F5). With MacDiff software, counts generated from treated and untreated specimens can be adjusted until

F5. Representative X-ray diffractograms, p. 23.

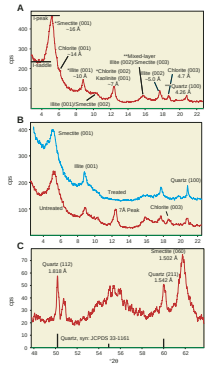

the peak area for quartz (100) is the same for both. The ratio of untreated to HCl-treated (and adjusted) 7-Å peak areas then serves as a measure of the kaolinite contribution.

Percent Illite in Mixed-Layer Illite/Smectite Clays

Several methods exist for the XRD determination of percent illite in I/S mixed-layer clays. Srodon (1980) and Watanabe (1988) based their methods on differences in the positions of key peaks; however, they do not work well for samples with discrete illite. Another common method (Rettke, 1981) is based on the ratio of intensity of the "saddle" at the low diffraction angles to intensity of the 17-Å peak (Fig. F5). This method can be advantageous when samples contain small amounts of expandable clay, but it ceases to work when expandability drops below 40%. Reynolds and Hower (1970) documented the angular separation between I(001)/S(002) and I(002)/S(003) peaks (Fig. F5) using a combination of synthetic and natural diffractograms. Hathon (1992) compared this and other methods by imaging clays with transmission electron microscopy (TEM) and found that the percent smectite as estimated by XRD analyses usually falls within ±5% of visual estimates by TEM. Error in XRD data increases with the addition of discrete illite.

The advantage of using angular separation between two peaks is the method's insensitivity to instrument misalignments and variations in thickness of the ethylene glycol layer (Moore and Reynolds, 1997). If concentrations of I/S are low, however, all of the mixed-layer peaks are difficult to resolve above background counts, and in many cases the I(001)/S(002) peak is completely obscured. Results calculated from d-values of the I(002)/S(003) peak will match those based on separation between the two I/S peaks if each profile is corrected for misalignments. MacDiff software accomplishes this by shifting the quartz (100) peak to a d-value of 4.26 Å (although sometimes the correction command must be repeated). For many of the samples that we analyzed, the I(002)/S(003) peak is broad and irregular because of poor crystallinity and mixing among several types of I/S. The center of each peak was picked for its d-value by assuming a symmetrical shape.

As the smectite–illite transition proceeds, the percentage of illite in the mixed-layer structure increases and the organization of I/S interlayers changes from random to ordered (Reynolds and Hower, 1970; Altaner and Ylagan, 1997). I/S clays are usually disordered with ≤50% illite, and $R = 1$ ordering typically occurs at 55%–60% illite. The development of ordering may be recognized by a shift of the second-order I/S superstructure from ~5° to 6.5°2θ (Moore and Reynolds, 1997). During processing of XRD data, we also checked the position of this reflection.

Smectite Type

We selected nine samples from Site 1173 and eight samples each from Sites 1174 and 1177 to identify the type of smectite. Because the (060) reflection is sensitive to the site occupancy and cation size in the octahedral sheet, its d-value allows dioctahedral varieties to be distinguished from trioctahedral varieties. The d(060) values for dioctahedral montmorillonite and beidellite are between 1.492 and 1.504 Å, whereas d-values for the trioctahedral forms (saponite and hectorite) and dioctahedral nontronite range from 1.520 to 1.530 Å (Brindley, 1980). Because (060) reflections are weak in most oriented clay aggregates, random powder mounts must be prepared. Portions of the <2-µm frac-

tion were freeze-dried, manually disaggregated to remove clumps, and pressed into holders, taking care to minimize orientation of the particles. Samples were scanned from 48° to 64°2θ at scan rate = 0.5°/min, step size = 0.01, voltage = 40 kV, and current = 30 mA. This scanning range includes a (112) quartz peak at 1.817 Å, which permits corrections for small offsets of the goniometer (Fig. F5). The corrected position of the quartz (211) peak can also be verified at 1.542 Å ± 0.001 Å. The center of the (060) smectite peak was used to obtain its d-value, checking the profiles in both the smoothed and unsmoothed form (Fig. F5).

RESULTS

Minerals in Clay-Sized Fraction

Site 1173

Smectite is, on average, the most abundant clay-sized mineral at Site 1173 (Table T1; Fig. F2), followed by illite and chlorite (+ kaolinite). Quartz makes up an average of 10 wt% of the <2-µm fraction. Smectite increases downhole from ~20 wt% at the top of the trench-wedge facies to >60 wt% near the top of the lower Shikoku Basin facies (~380 mbsf); from there, smectite gradually decreases to ~35 wt%. The abundance of smectite is erratic in the volcaniclastic facies, ranging from 16 to 82 wt%. The d(060) value ranges from 1.499 to 1.502 Å, demonstrating that the smectite is dioctahedral; it is unknown if the mineral is montmorillonite, beidellite, or a transitional member. As smectite increases in relative abundance, illite declines from ~40 wt% in the trench-wedge facies to ~25 wt% near 380 mbsf in the lower Shikoku Basin facies. Illite then increases to ~35 wt% in two intervals: near 430 mbsf and between 440 and 520 mbsf (Fig. F2). Illite fluctuates erratically in the volaniclastic facies. Chlorite (+ kaolinite) decreases from ~30 wt% at the top of the trench-wedge facies and to ~2 wt% by 380 mbsf. Values increase to ~25 wt% by 400 mbsf and remain fairly consistent to the top of the volcaniclastic facies. Two samples from the lower Shikoku Basin facies show that kaolinite contributes 0% and 12% to the 7-Å peak area (Table T2).

Composite peaks from mixed-layer illite/smectite clays were not detected consistently in samples from above 270 mbsf (Table T1). Starting at 350 mbsf, the percent illite in I/S clays increases from ~15% to 50%, with a maximum of 61%, but there is considerable scatter in the values (Fig. F6). Based on the position of the second-order superstructure, the smectite is disordered. The saddle/peak method does not show any clearly defined changes in I/S with depth (Table T1).

Site 1174

On average, illite and smectite are present in nearly equal amounts at Site 1174 (Table T1; Fig. F3), followed in abundance by chlorite (+ kaolinite). The relative abundance of quartz averages 12 wt%. Smectite abundance increases downhole from ~20 to >55 wt% near 600 mbsf; it then decreases to ~20 wt% by 1100 mbsf. The smectite is dioctahedral, with d(060) values between 1.499 and 1.503 Å. Illite declines from ~35 wt% at the top of the hole to 25 wt% near 650 mbsf. There is a small increase to 35–40 wt% toward the base of the hole. Chlorite (+ kaolinite)

T1. X-ray diffraction analysis, p. 27.

T2. Comparison of 7-Å peaks, p. 36.

F6. Illite in I/S mixed-layer clays, p. 24.

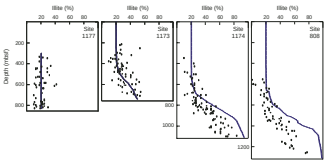

decreases from 25 wt% near top of the hole to 10 wt% at ~660 mbsf, then increases below 840 mbsf. The illitic component of I/S mixed-layer clay increases consistently below 590 mbsf, reaching a maximum of 89% (Fig. F6). The gradient in illitization is more pronounced at this site than at Site 1173, but R = 1 ordering does not occur. The saddle/peak method indicates an increase to 45% illite (at 1090 mbsf) (Table T1).

Site 1177

The average relative abundance of smectite at Site 1177 is 51 wt% (Table T1; Fig. F4). Illite averages 27 wt%, chlorite (+ kaolinite) averages 12 wt%, and quartz 11 wt%. The lower Shikoku Basin turbidite facies displays a degree of compositional scatter that is consistent with its lithologic heterogeneity (interbedded turbidites and hemipelagic mudstone). The amount of smectite increases from ~25 wt% at 300 mbsf (upper Shikoku Basin facies) to ~45 wt% at 570 mbsf. Between 570 mbsf and the volcaniclastic-rich facies, smectite varies from 30 to 87 wt%. Smectite content is also erratic in the volcaniclastic-rich facies (27–91 wt%). The smectite is dioctahedral, with d(060) values of 1.499 to 1.503 Å. Illite decreases from ~35 to 20 wt% by 700 mbsf then remains between 15 and 20 wt% to the base of the lower Shikoku Basin turbidites. Chlorite (+ kaolinite) declines from 25 wt% at 300 mbsf to <10 wt% at the base. Based on two samples, kaolinite contributions to the 7-Å peak area are 28% and 60% (Table T2). The I/S mixed-layer clays show no pattern of systematic change with depth (Fig. F6). The percent illite in I/S clays reaches a maximum of 42%, but most values are <25% with random ordering (Table T1).

Smectite Abundance in Bulk Mudstone

Placing the clay mineral data in the context of bulk mineralogy is beneficial if the goal is to evaluate whether smectite affects the mechanical and hydrologic properties of the Nankai accretionary prism. To do this, we multiplied the abundance of total clay minerals (using data from the nearest bulk powder sample interval) by the relative weight percent of smectite in the <2-µm clay mineral fraction (where smectite + illite + chlorite = 100%). Although bulk powder XRD methods are imperfect, error analysis shows that the SVD method is accurate to within 5 wt% for standard mineral mixtures (Shipboard Scientific Party, 2001a; **Underwood et al.,** this volume). Nevertheless, our calculated values of mineral abundance in the bulk sediment do not take into account the presence of amorphous solids (e.g., volcanic glass and biogenic silica), and the value calculated for total clay is relative only to quartz, feldspar, and calcite. In addition, clay-fraction data may be affected by mineral partitioning as a function of grain size; this can increase the concentration of smectite in finer size fractions as compared to silt-sized contributions of detrital illite and chlorite (e.g., Mitchell, 1993). Using the <2-µm size fraction probably overestimates the abundance of smectite in bulk mudstone, so the values we report should be considered as maxima for comparative purposes.

Aside from local "spikes" of smectite associated with thin volcanic ash layers, the abundance of smectite in bulk mudstone from Sites 1173 and 1174 is generally <30 wt% (Fig. F7). Depletion of smectite is more extensive in the lower Shikoku Basin deposits at Site 1174. Mudstones from Site 1177, in contrast, contain >30 wt% smectite at virtually all

F7. Smectite in bulk mudstone, p. 25.

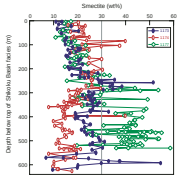

depths in the lower Shikoku Basin facies and volcaniclastic-rich facies; values reach 40–55 wt% near the base of the hole (Fig. F7). The differences in smectite content among coeval deposits at the three sites are probably due to variable amounts of ash-to-smectite and smectite–illite diagenesis.

Modeling Illite–Smectite Reaction Progress

Many factors influence the smectite–illite reaction, including temperature, potassium concentration in pore water, time, water/rock ratio, fluid and rock composition, the starting composition of the mixed-layer clay, and pressure (Pollastro, 1993, and references therein). The most important of these factors are temperature, heating time, and potassium availability. In one experimentally derived kinetic model, Huang et al. (1993) solved the conversion rate as follows:

$$-(dS/dt) = Ae^{-E\alpha/RT}[K^+]S^2,$$

where,

S = fraction of smectite in the I/S clays,
t = time,
A = frequency factor (8.08×10^{-4}/s),
E_α = activation energy (28 kcal/mole),
R = gas constant,
T = temperature (Kelvin), and
K^+ = concentration of potassium (in molarity).

We used this kinetic model to predict the smectite–illite conversion by simulating the evolution of a single packet of smectite as it is buried. Using constraints from shipboard data, calculations were completed at 10-m intervals for Sites 808, 1173, 1174, and 1177.

Model Inputs

The assumed starting value for percent illite in I/S was set at 20% illite for each ODP site on the basis of data from shallow burial depths where diagenesis has not yet occurred (Fig. F6). Age-depth relations at each site are sensitive to variations in sedimentation rate and thrusting at the prism toe, so nonuniform burial rates were input into the model. Our choices for age-depth inputs (Table T3) are constrained by paleomagnetic and nannofossil data (Shipboard Scientific Party, 1991, 2001c, 2001d, 2001e; Olafsson, 1993). The potassium concentration for each 10-m interval was taken from the nearest shipboard pore fluid measurement (Shipboard Scientific Party, 1991, 2001c, 2001d, 2001e). Those choices make no allowances for the likelihood of potassium depletion or enrichment through time in response to fluid migration along faults, diffuse flow during consolidation, or in situ mineral reactions. The present-day temperature at each model depth was estimated from shipboard thermal conductivity data and heat flow calculations (Shipboard Scientific Party, 1991, 2001c, 2001d, 2001e; Fisher et al., 1993; Kinoshita and Yamano, 1996). We used a heat flow value of 180 mW/m² for Sites 1173, 1174, and 808, but a much lower value of 63 mW/m² was used for Site 1177. We assumed purely vertical conductive and steady-state heat flow, so the modeling ignores the likely effects of thermal de-

T3. Kinetic modeling of smectite–illite reaction progress, p. 37.

cay following the cessation of volcanism along the spreading ridge of Shikoku Basin (Wang et al., 1995).

Model Results

Figure F6 shows that maximum diagenetic alteration of sediments at Sites 1174 and 808 is less advanced than what model predictions indicate by ~15%–20%. According to one iteration of the kinetic model, illite–smectite diagenesis should reach 94% illite at the base of Hole 1174B, but the maximum illite value measured for the <2-µm size fraction is 84%. At Site 808, illite should reach 98% by the base, but the measured maximum is 78%. This mismatch may be due to rapid tectonic thickening and thrusting near the deformation front, as discussed subsequently. Predictions for Site 1173 are in better general agreement with the observations. The lower temperature gradient at Site 1177 obviously retards the illite–smectite reaction, and modeling predicts no reaction progress (Fig. F6). The calculated geotherm of 53°C/km yields a temperature projection of only 44°C at the base of the hole. The onset of illitization generally occurs between 58° and 92°C (Freed and Peacor, 1989b). Thus, we believe that all of the I/S at Site 1177 is detrital in origin.

DISCUSSION

Detrital Provenance

The Izu-Honshu collision zone of central Japan has been identified as the detrital source of the Quaternary trench-wedge facies on the basis of sand petrography, paleoflow indicators, facies architecture, clay mineral assemblages, and detailed characterization of the detrital illite component (Taira and Niitsuma, 1986; Marsaglia et al., 1992; Pickering et al., 1992; Taira and Ashi, 1993; Underwood et al., 1993a; **Fergusson,** this volume). Clay mineral assemblages change, however, in older deposits of the Shikoku Basin. As discussed below, some of those changes probably resulted from diagenetic reactions but diagenesis is superimposed on temporal shifts in the detrital inputs. Dispersal systems for suspended sediment sometimes fluctuate in response to dispersal mechanisms (i.e., surface currents and pathways of sediment gravity flow), uplift of new source areas, climatic controls over the degree of chemical vs. physical weathering, or changes in the amount of exposed volcanic material in a given source. As described by **Underwood and Steurer** (this volume), we now have enough evidence from ODP sites that have not been affected by diagenesis to reconstruct the temporal evolution of the regional-scale dispersal system for Nankai Trough and Shikoku Basin.

As one moves upsection from the lower to upper Shikoku Basin facies, the increase of wind-blown volcanic ash layers suggests that explosive volcanism gradually intensified from the early Pliocene into the Quaternary. Although the source for each ash layer remains uncertain, contributions could have come from volcanoes on Kyushu, central to northern Honshu, and/or the Izu-Bonin island arc (Cambray et al., 1995; Uto and Tatsumi, 1996; Kamata and Kodama, 1999). Working farther seaward in coeval Shikoku Basin deposits, Chamley (1980) documented a gradual decrease of smectite in progressively younger mudstones. Stratigraphic trends at Site 1177 are more erratic due to the

prevalence of turbidites in the lower Shikoku Basin, but the same overall pattern of decreasing smectite through time holds there (Fig. F4). In addition, the content of smectite is relatively high in late Miocene and Pliocene trench-slope sediments at Site 1178 (**Underwood and Steurer,** this volume).

These data create an interesting paradox: the relative abundance of smectite in mudstone, which forms primarily by weathering of volcanic source rocks, decreases basinwide during the same period of time in which interbedded ash layers become more plentiful. To explain this observation, **Underwood and Steurer** (this volume) linked the gradual depletion of detrital smectite to intensification of the Kuroshio Current at ~3 Ma; that change in surface water circulation occurred in response to closure of the Pacific-Caribbean Gateway. A stronger and deeper surface current, flowing toward the northeast, would be expected to dampen the transfer of suspended sediment from the Izu-Bonin volcanic source and increase the amount of illite and chlorite carried into the Shikoku Basin and Nankai Trough from the Outer Zone of Japan. It is also interesting to note that simultaneous intensification of the Tsushima Current in the Sea of Japan (i.e., during the Pliocene) evidently caused a similar shift toward higher percentages of illite and chlorite at the expense of smectite (Fagel et al., 1992).

Clay Diagenesis

Several lines of evidence show that diagenetic reactions are superimposed on the inferred temporal shifts in the detrital flux into Shikoku Basin. Alteration of volcanic glass to clay minerals is readily apparent in smear slides, for example, and the total clay content in bulk powders increases as the glass degenerates (Shipboard Scientific Party, 2001c, 2001d; **Wilson et al.,** this volume). Masuda et al. (1996) imaged volcanic glass shards from Site 808 with TEM and saw progressive growth of smectite crystals with dioctahedral beidelitic composition. "Spikes" in smectite content of up to 91 wt% occur locally in the Shikoku Basin deposits (Figs. F2, F3); these unusually high values probably come from in situ alteration of volcanic ash layers, although the cryptic bentonites did not stand out from surrounding sediment during visual inspection. Similarly, at Site 1177, sporadic increases in total smectite in the lower Shikoku Basin turbidite facies (Figs. F4, F6) seem too large to attribute exclusively to fluctuating detrital sources. We suggest that replacement of disseminated glass shards in the Miocene mudstone deposits added authigenic smectite to what were already high detrital contributions of both discrete smectite and disordered I/S mixed-layer clay.

Site 1173, the so-called reference site for the Muroto Transect, experienced diagenetic alteration seaward of the deformation front. Illite–smectite reaction progress clearly advances from Site 1173 landward to Site 1174 (Fig. F6). Smectite–illite diagenesis begins at ~390 mbsf at Site 1173 and at ~700 mbsf at Site 1174. At progressively deeper intervals, the percent illite in I/S clays increases (Fig. F6) and the content of smectite remaining in bulk mudstones decreases (Fig. F7). Larger amounts of scatter in I/S proportions at Site 1173 are probably due to mixing between detrital I/S and authigenic I/S. The gradient for Site 1174 is more pronounced because the diagenetic overprint is more extensive. The smectite–illite transition does not reach completion, however, which is consistent with the results from Site 808 (Underwood et al., 1993b). At Site 1174, the maximum illite in I/S is 84%, but there is no evidence of $R = 1$ ordering. At Site 1173, the maximum illite in I/S is 55%, with no

ordering. A transition from $R = 0$ to $R = 1$ is supposed to occur when the illite interlayers in I/S reach 60%–70% (Bethke et al., 1986). In older basins this transition occurs at ~100° to 110°C, whereas in younger basins subjected to rapid heating (<3 Ma) this transition is not expected until ~120° to 140°C (Pollastro, 1993). $R = 1$ ordering was noted at Site 808 at 1220 mbsf and an inferred temperature of 135°C (Underwood et al., 1993b), but newer heat flow data (Shipboard Scientific Party 2001c, 2001d) push that temperature estimate to 144°C.

Figure F8 shows how sensitive the numerical simulations of illite–smectite reaction progress are to changes in potassium concentration, burial rate, and heat flow. Variations in heat flow produce the largest changes in the model results. If heat flow at Site 1173 is lowered to 130 mW/m² or less, the model predicts that smectite–illite diagenesis will not even initiate. At Site 1174, heat flow must be reduced to 70 mW/m² to prevent initiation of illite–smectite diagenesis, but using the documented heat flow value of 180 mW/m² overpredicts reaction progress by 15%–20%. Evidently, reaction progress has been retarded either by fluid composition or by insufficient heating time. Present-day potassium concentrations at Sites 1173, 1174, and 808 are more than sufficient to promote the observed reaction progress (Fig. F8). Changing the potassium concentration to minimum values at each site (Site 1173 = 1.8 mM and Site 1174 = 1.5 mM) does not change the model result very much (Fig. F8). Thus, it appears as though potassium has been plentiful enough throughout the basin's burial history. Conversely, increasing the potassium concentration to the maximum value for each site (i.e., normal bottom water) substantially overpredicts the illite–smectite transformation. This scenario is unlikely, however, because it requires continual replenishment of dissolved potassium from an outside source. Changing the age-depth constraints that are listed in Table T3 to more straightforward linear burial gradients results in modest adjustments of the model (Fig. F8). To mimic the effects of faster burial, we reduced the age at each interval by specified percentages; an adjustment of 50% improves the fit between the model prediction and measured values at Site 1174. From this result, we conclude that recent episodes of burial near the toe of the Nankai accretionary prism (i.e., by trench-axis sedimentation, tectonic thickening, and frontal thrusting) may have been too fast for the illite–smectite reaction to keep pace. More sophisticated modeling will be required to explore how reaction progress responded to both gradual and punctuated shifts in heat flow, fluid flow, and burial rates (e.g., Wang et al., 1995; Saffer and Bekins, 1999).

F8. Sensitivity analysis for the smectite–illite kinetic model, p. 26.

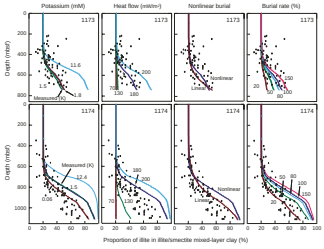

Effects of Clay on Geotechnical Properties

Hyndman et al. (1995) demonstrated that the updip limit of earthquakes along the Nankai subduction boundary occurs within a temperature window of 100°–150°C. Diagenetic changes in clay minerals are noteworthy in this context because of a hypothesized link between fault zone strength and thermally controlled mineral reactions. Vrolijk (1990), for example, speculated that the updip limit of seismicity matches the depth where 80% of the incoming smectite is transformed to a stronger illite-rich clay assemblage. Smectite has been shown to affect the sliding behavior of faults. In experiments on artificial montmorillonite anhydrite gouges, Shimamoto and Logan (1981) discovered that a bulk content of 15%–20% smectite changes stick-slip behavior to stable sliding. The coefficient of internal friction for natural smectite-bearing gouges from the San Andreas fault zone ranges from 0.21 to

0.41 (Morrow et al., 1982). Logan and Rauenzahn (1987) found that the frictional coefficient for pure montmorillonite ranges from 0.08 to 0.14, whereas the coefficient for quartz gouge ranges from 0.49 to 0.62. In a two-component mixture of quartz + smectite, the weaker mineral must exceed 25% of the bulk total to cause a significant reduction of the coefficient of friction (Logan and Rauenzahn, 1987).

Influenced by such laboratory results, Moore and Saffer (2001) discussed how the transformation of mudstones with initial contents of 30%–50% smectite might lead to changes in frictional properties downdip, but they also pointed out that incoming sediment along the Muroto Transect does not contain enough smectite to create such a scenario by itself. They cited, instead, contributions imparted on frictional properties and effective stress by increases in fluid pressure, hydrocarbon maturation, opal-A to opal-CT transformation, pressure solution, and cementation by zeolites, calcite, phyllosilicates, and silica, all of which occur over the temperature range of 100°–150°C. The logic of Moore and Saffer (2001) certainly holds for strata at Sites 808 and 1174. On the other hand, along the Ashizuri Transect (Site 1177), mudstones in the lower Shikoku Basin turbidite facies and volcaniclastic-rich facies are enriched by much higher percentages of smectite (Fig. F7). The geotechnical response to smectite–illite diagenesis is probably greater landward of the deformation front in the Ashizuri region.

Other geotechnical properties are affected by relatively small amounts of smectite. Robinson and Allam (1998) found that the coefficient of consolidation for montmorillonite decreases with increasing consolidation pressure, whereas other clays show increases in the coefficient with increasing pressure. The coefficient of consolidation also decreases as the proportion of smectite increases (Abeele, 1986). Adding as little as 5% smectite to silty sand increases compressibility, decreases shear strength, and increases secondary compression (Santucci de Magistris et al., 1998). Permeability is likewise affected by small amounts of smectite. In one study, hydraulic conductivity in a mixture of 6% smectite plus sandy silts was nearly equal to that of pure bentonite (Abeele, 1986). Freed and Peacor (1989a) showed that illite packets growing in the smectite matrix in I/S clays reduce the local permeability. In addition, the release of interlayer water during the smectite–illite transition can contribute to excess pore fluid pressures (Bruce, 1984; Colten-Bradley, 1987). Thus, even along corridors where the initial smectite content is not plentiful enough (i.e., <30 wt%) to change the rock's frictional coefficient during illite–smectite diagenesis, expandable clay affects compressibility, fluid migration, and effective stress along the Nankai-Shikoku subduction zone.

CONCLUSIONS

On average, smectite is the most abundant mineral in the clay-sized fraction at Sites 1173 and 1177, followed by illite and chlorite (+ kaolinite). At Site 1174, illite is the most abundant clay mineral, followed by smectite and chlorite (+ kaolinite). The smectite is dioctahedral, which is consistent with its origin as an alteration product of silicic volcanic rock and ash.

Data from Sites 1173, 1174, and 1177 show downhole increases of smectite in Shikoku Basin deposits. Part of this increase was caused by changes in detrital influx. The transfer of smectite to Shikoku Basin and Nankai Trough was higher during the Miocene and decreased progres-

sively through the Pliocene and Quaternary. In situ alteration of disseminated volcanic glass added even more authigenic smectite to the clay assemblage as burial depths and temperatures gradually increased.

Data from Sites 1173 and 1174 show downhole depletions of smectite in the lower Shikoku Basin deposits over the same depth ranges as increasing percentages of illite in I/S mixed-layer clays. An absence of this reaction at Site 1777 is consistent with its lower geothermal gradient. A kinetic model of illite–smectite reaction progress matches the diagenetic profile for Site 1173 fairly well using the present-day values of temperature, burial time, and potassium availability. Modeling indicates that rapid burial and/or tectonic thickening at Sites 1174 and 808 caused illite–smectite diagenesis to lag behind the prevailing temperature conditions by 15%–20%.

The maximum abundance of bulk smectite in mudstones from Site 1173 is ~35 wt%; at Site 1174 the maximum reaches nearly 30 wt%. Most such values, however, are <25 wt%. Mudstones from Site 1177 (Ashizuri Transect) are significantly different because bulk smectite consistently reaches 30–50 wt%, especially in the lower Shikoku Basin. This amount of smectite should be enough to lower the coefficient of friction of the sediment relative to coeval deposits in the Muroto Transect. Smectite probably affects mudstone compressibility and permeability at all three sites.

ACKNOWLEDGMENTS

We thank Captain Tom Ribbens, the crew, technicians, and fellow scientists aboard *JOIDES Resolution* for their dedicated assistance during ODP Leg 190. We thank Nathalie Fagel and an anonymous reviewer for their helpful comments and insights. This research used samples provided by the Ocean Drilling Program (ODP). ODP is sponsored by the U.S. National Science Foundation (NSF) and participating countries under management of Joint Oceanographic Institutions (JOI), Inc. Funding was provided by a Schlanger Ocean Drilling Fellowship to J. Steurer and the U.S. Science Support Program (grant F001281 to M. Underwood). Arpit Ghoting, Anup Bidesi, Nandini Basu, Swati Udas, Eric Grabowski, Marcie Workman, and Burt Thomas assisted with sample preparation.

REFERENCES

Abeele, W.V., 1986. The influence of bentonite on the permeability of sandy silts. *Nucl. Chem. Waste Manage.,* 6:81–88.

Altaner, S.P., and Ylagan, R.F., 1997. Comparison of structural models of mixed-layer illite/smectite and reaction mechanisms of smectite illitization. *Clays Clay Miner.,* 45:517–533.

Bethke, C.M., Vergo, N., and Altaner, S.P., 1986. Pathways of smectite illitization. *Clays Clay Miner.,* 34:125–135.

Bird, P., 1984. Hydration-phase diagrams and friction of montmorillonite under laboratory and geologic conditions, with implications for shale compaction, slope stability, and strength of fault gouge. *Tectonophysics,* 107:235–260.

Biscaye, P.E., 1965. Mineralogy and sedimentation of recent deep-sea clays in the Atlantic Ocean and adjacent seas and oceans. *Geol. Soc. Am. Bull.,* 76:803–832.

Brindley, G.W., 1980. Order-disorder in clay mineral structures. *In* Brindley, G.W., and Brown, G. (Eds.), *Crystal Structures of Clay Minerals and Their X-Ray Identification*. Mineral. Soc. Monogr., 5:125–195.

Bruce, C.H., 1984. Smectite dehydration—its relation to structural development and hydrocarbon accumulation in northern Gulf of Mexico basin. *AAPG Bull.,* 68:673–683.

Burst, J.F., 1969. Diagenesis of Gulf Coast clayey sediments and its possible relation to petroleum migration. *AAPG Bull.,* 53:73–93.

Cambray, H., Pubellier, M., Jolivet, L., and Pouclet, A., 1995. Volcanic activity recorded in deep-sea sediments and the geodynamic evolution of western Pacific island arcs. *In* Taylor, B., and Natland, J. (Eds.), *Active Margins and Marginal Basins of the Western Pacific*. Geophys. Monogr., 88:97–124.

Chamley, H., 1980. Clay sedimentation and paleoenvironment in the Shikoku Basin since the middle Miocene (Deep Sea Drilling Project Leg 58, North Philippine Sea). *In* Klein, G. de V., Kobayashi, K., et al., *Init. Repts. DSDP,* 58: Washington (U.S. Govt. Printing Office), 669–678.

————, 1989. *Clay Sedimentology:* Berlin (Springer-Verlag).

Chamley, H., Cadet, J.-P., and Charvet, J., 1986. Nankai Trough and Japan Trench late Cenozoic paleoenvironments deduced from clay mineralogic data. *In* Kagami, H., Karig, D.E., Coulbourn, W.T., et al., *Init. Repts. DSDP,* 87: Washington (U.S. Govt. Printing Office), 633–641.

Colten-Bradley, V.A., 1987. Role of pressure in smectite dehydration—effects on geopressure and smectite-to-illite transformation. *AAPG Bull.,* 71:1414–1427.

Cook, H.E., Zemmels, I., and Matti, J.C., 1975. X-ray mineralogy data, far western Pacific, Leg 31 Deep Sea Drilling Project. *In* Karig, D.E., Ingle, J.C., Jr., et al., *Init. Repts. DSDP,* 31: Washington (U.S. Govt. Printing Office), 883–895.

Dickinson, W.R., and Seely, D.R., 1979. Structure and stratigraphy of forearc regions. *AAPG Bull.,* 63:2–31.

Fagel, N., Andre, L., Chamley, H., Debrabant, P., and Jolivet, L., 1992. Clay sedimentation in the Sea of Japan since the early Miocene: influence of source-rock and hydrothermal activity. *Sediment. Geol.,* 80:27–40.

Fagel, N., Robert, C., Preda, M., and Thorez, J., 2001. Smectite composition as a tracer of deep circulation: the case of the northern North Atlantic. *Mar. Geol.,* 172:309–330.

Faugeres, J.C., Gonthier, E., Masse, L., Parra, M., Pons, J.C., and Pujol, C., 1991. Quaternary deposits on the South Barbados accretionary prism. *Mar. Geol.*, 96:247–267.

Fisher, A.T., Foucher, J.P., Yamano, M., and Hyndman, R., 1993. *Data report:* Corrected thermal conductivity data, Leg 131. *In* Hill, I.A., Taira, A., Firth, J.V., et al., *Proc. ODP, Sci. Results,* 131: College Station, TX (Ocean Drilling Program), 451–456.

Fisher, A.T., and Underwood, M.B., 1995. Calibration of an X-ray diffraction method to determine relative mineral abundances in bulk powders using matrix singular

value decomposition: a test from the Barbados accretionary complex. *In* Shipley, T.H., Ogawa, Y., Blum, P., et al., *Proc. ODP, Init. Repts.,* 156: College Station, TX (Ocean Drilling Program), 29–37.

Freed, R.L., and Peacor, D.R., 1989a. Geopressured shale and sealing effect of smectite to illite transition. *AAPG Bull.,* 73:1223–1232.

————, 1989b. Variability in temperature of the smectite/illite reaction in Gulf Coast sediments. *Clay Miner.,* 24:171–180.

Hathon, E.G., 1992. X-ray diffraction and transmission electron microscopy study of the surface charge on the illite and smectite components of illite/smectite mixed-layer clays [Ph.D. dissert.]. Univ. of Missouri, Columbia.

Hathon, E.G., and Underwood, M.B., 1991. Clay mineralogy and chemistry as indicators of hemipelagic sediment dispersal south of the Aleutian arc. *Mar. Geol.,* 97:145–166.

Hein, J.R., Yeh, H.-W., and Alexander, E., 1979. Origin of iron-rich montmorillonnite from the manganese nodule belt of the north equatorial pacific. *Clays Clay Miner.,* 27:185–194.

Hower, J., Eslinger, E.V., Hower, M.E., and Perry, E.A., 1976. Mechanism of burial metamorphism of argillaceous sediment. 1. Mineralogical and chemical evidence. *Geol. Soc. Am. Bull.,* 87:725–737.

Huang, W.-L., Longo, J.M., and Pevear, D.R., 1993. An experimentally derived kinetic model for smectite-to-illite conversion and its use as a geothermometer. *Clays Clay Miner.,* 41:162–177.

Hyndman, R.D., Wang, K., and Yamano, M., 1995. Thermal constraints on the seismogenic portion of the southwestern Japan subduction thrust. *J. Geophys. Res.,* 100:15373–15392.

Kamata, H., and Kodama, K., 1999. Volcanic history and tectonics of the southwest Japan arc. *Isl. Arc*, 8:393–403.

Kastner, M., Elderfield, H., and Martin, J.B., 1991. Fluids in convergent margins: what do we know about their composition, origin, role in diagenesis and importance for oceanic chemical fluxes? *Philos. Trans. R. Soc. London, Ser. A,* 335:243–259.

Kinoshita, H., and Yamano, M., 1986. The heat flow anomaly in the Nankai Trough area. *In* Kagami, H., Karig, D.E., Coulbourn, W.T., et al., *Init. Repts DSDP,* 87: Washington (U.S. Govt. Printing Office), 737–743.

Logan, J.M., and Rauenzahn, K.A., 1987. Frictional dependence of gouge mixtures of quartz and montmorillonite on velocity, composition and fabric. *Tectonophysics,* 144:87–108.

Marsaglia, K.M., Ingersoll, R.V., and Packer, B.M., 1992. Tectonic evolution of the Japanese Islands as reflected in modal compositions of Cenozoic forearc and backarc sand and sandstone. *Tectonics,* 11:1028–1044.

Masuda, H., O'Neil, J.R., Jiang, W.T., and Peacor, D.R., 1996. Relation between interlayer composition of authigenic smectite, mineral assemblages, I/S reaction rate and fluid composition in silicic ash of the Nankai Trough. *Clays Clay Miner.*, 44:443–459.

Masuda, H., Peacor, D.R., and Dong, H., 2001. Transmission electron microscopy study of conversion of smectite to illite in mudstones of the Nankai Trough: contrast with coeval bentonites. *Clays Clay Miner.,* 49:109–118.

Mitchell, J.K., 1993. *Fundamentals of Soil Behavior* (2nd ed.): New York (Wiley).

Moore, D.M., and Reynolds, R.C., Jr., 1997. *X-Ray Diffraction and the Identification and Analysis of Clay Minerals* (2nd ed.): New York (Oxford Univ. Press).

Moore, G.F., Taira, A., Klaus, A., and Leg 190 Scientific party, 2001. New insights into deformation and fluid flow processes in the Nankai Trough accretionary prism: Results of Ocean Drilling Program Leg 190. *Geochem. Geophys. Geosyst.,* 2:10.1029/2001GC000166.

Moore, J.C., and Saffer, D.M., 2001. Updip limit of the seismogenic zone beneath the accretionary prism of southwest Japan: an effect of diagenetic to low-grade metamorphic processes and increasing effective stress. *Geology,* 29:183–186.

Moore, J.C., and Vrolijk, P., 1992. Fluids in accretionary prisms. *Rev. Geophys.,* 30:113–135.

Morrow, C.A., Shi, L.Q., and Byerlee, J.D., 1982. Strain hardening and strength of clay-rich fault gouges. *J. Geophys. Res.,* 87:6771–6780.

————, 1984. Permeability of fault gouge under confining pressure and shear stress. *J. Geophys. Res.,* 89:3193–3200.

Naidu, A.S., and Mowatt, T.C., 1983. Sources and dispersal patterns of clay minerals in surface sediments from the continental-shelf areas off Alaska. *Geol. Soc. Am. Bull.,* 94:841–854.

Olafsson, G., 1993. Calcareous nannofossil biostratigraphy of the Nankai Trough. *In* Hill, I.A., Taira, A., Firth, J.V., et al., *Proc. ODP, Sci. Results,* 131: College Station, TX (Ocean Drilling Program), 3–13.

Olson, R.E., 1974. Shearing strength of kaolinite, illite, and montmorillonite, *J. Soil Mech. Found. Eng.-ASCE*, 100:1215–1229.

Orr, R.M., 1992. Clay mineralogy, diagenesis, and provenance of sediments in the Nankai Trough, offshore Shikoku Island, southwest Japan [M.S. thesis]. Univ. of Missouri, Columbia.

Perry, E., and Hower, J., 1970. Burial diagenesis in Gulf Coast pelitic sediments. *Clays Clay Miner.,* 18:165–177.

Petschick, R., 2001. MacDiff software v. 4.2.5 [Online]. Available from the World Wide Web: <http://servermac.geologie.uni-frankfurt.de/Staff/Homepages/Petschick/RainerE.html>. [Cited 2002-11-9]

Petschick, R., Kuhn, G., and Gingele, F., 1996. Clay mineral distribution in surface sediments of the South Atlantic: sources, transport, and relation to oceanography. *Mar. Geol.,* 130:203–229.

Pickering, K.T., Underwood, M.B., and Taira, A., 1992. Open-ocean to trench turbidity-current flow in the Nankai Trough: Flow collapse and reflection. *Geology,* 20:1099–1102.

————, 1993. Stratigraphic synthesis of the DSDP-ODP sites in the Shikoku Basin, Nankai Trough, and accretionary prism. *In* Hill, I.A., Taira, A., Firth, J.V., et al., *Proc. ODP, Sci. Results,* 131: College Station, TX (Ocean Drilling Program), 313–330.

Piper, D.J.W., von Huene, R., and Duncan, J.R., 1973. Late Quaternary sedimentation in the active eastern Aleutian Trench. *Geology,* 1:19–22.

Pollastro, R.M., 1993. Considerations and applications of the illite/smectite geothermometer in hydrocarbon-bearing rocks of Miocene to Mississippian age. *Clays Clay Miner.,* 41:119–133.

Porter, S., Vanko, D.A., and Ghazi, A.M., 2000. Major and trace element compositions of secondary clays in basalts altered at low temperature, eastern flank of the Juan de Fuca Ridge. *In* Fisher, A., Davis, E.E., and Escutia, C. (Eds.), *Proc. ODP, Sci. Results,* 168: College Station, TX (Ocean Drilling Program), 149–157.

Rettke, R.C., 1981. Probable burial diagenetic and provenance effects on Dakota Group clay mineralogy, Denver Basin. *J. Sediment. Petrol.,* 51:541–551.

Reynolds, R.C., and Hower, J., 1970. The nature of interlayering in mixed-layer illite-montmorillonites. *Clays Clay Miner.,* 18:25–36.

Robinson, R.G., and Allam, M.M., 1998. Effect of clay mineralogy on coefficient of consolidation. *Clays Clay Miner.,* 46:596–600.

Saffer, D.M., and Bekins, B.A., 1999. Fluid budgets at convergent plate margins: implications for the extent and duration of fault-zone dilation. *Geology,* 27:1095–1098.

Santucci de Magistris, F., Silvestri, F., and Vinale, F., 1998. Physical and mechanical properties of a compacted silty sand with low bentonite fraction. *Can. Geotech. J.,* 35:909–925.

Shimamoto, T., and Logan, J.M., 1981. Effects of simulated clay gouges on the sliding behavior of Tennessee sandstone. *Tectonophysics,* 75:243–255.

Shipboard Scientific Party, 1986. Site 582. *In* Kagami, H., Karig, D.E., Coulbourn, W.T., et al., *Init. Repts. DSDP,* 87: Washington (U.S. Govt. Printing Office), 35–122.

————, 1991. Site 808. *In* Taira, A., Hill, I., Firth, J.V., et al., *Proc. ODP, Init. Repts.,* 131: College Station, TX (Ocean Drilling Program), 71–269.

————, 2001a. Explanatory notes. *In* Moore, G.F., Taira, A., Klaus, A., et al., *Proc. ODP, Init. Repts.,* 190, 1–51 [CD-ROM]. Available from: Ocean Drilling Program, Texas A&M University, College Station TX 77845-9547, USA.

————, 2001b. Leg 190 summary. *In* Moore, G.F., Taira, A., Klaus, A., et al., *Proc. ODP, Init. Repts.,* 190: College Station TX (Ocean Drilling Program), 1–87.

————, 2001c. Site 1173. *In* Moore, G.F., Taira, A., Klaus, A., et al., *Proc. ODP, Init. Repts.,* 190, 1–147 [CD-ROM]. Available from: Ocean Drilling Program, Texas A&M University, College Station TX 77845-9547, USA.

————, 2001d. Site 1174. *In* Moore, G., Taira, A., Klaus, A., et al., *Proc. ODP, Init. Repts.,* 190, 1–149 [CD-ROM]. Available from: Ocean Drilling Program, Texas A&M University, College Station TX 77845-9547, USA.

————, 2001e. Site 1177. *In* Moore, G.F., Taira, A., Klaus, A., et al., *Proc. ODP, Init. Repts.,* 190, 1–91 [CD-ROM]. Available from: Ocean Drilling Program, Texas A&M University, College Station TX 77845-9547, USA.

Srodon, J., 1980. Precise identification of illite/smectite interstratifications by X-ray powder diffraction. *Clays Clay Miner.,* 28:401–411.

Taira, A., and Ashi, J., 1993. Sedimentary facies evolution of the Nankai forearc and its implications for the growth of the Shimanto accretionary prism. *In* Hill, I.A., Taira, A., Firth, J.V., et al., *Proc. ODP, Sci. Results,* 131: College Station, TX (Ocean Drilling Program), 331–341.

Taira, A., Hill, I., Firth, J., Berner, U., Brückmann, W., Byrne, T., Chabernaud, T., Fisher, A., Foucher, J.-P., Gamo, T., Gieskes, J., Hyndman, R., Karig, D., Kastner, M., Kato, Y., Lallement, S., Lu, R., Maltman, A., Moore, G., Moran, K., Olaffson, G., Owens, W., Pickering, K., Siena, F., Taylor, E., Underwood, M., Wilkinson, C., Yamano, M., and Zhang, J., 1992. Sediment deformation and hydrogeology of the Nankai accretionary prism: synthesis of shipboard results of ODP Leg 131. *Earth Planet. Sci. Lett.,* 109:431–450.

Taira, A., and Niitsuma, N., 1986. Turbidite sedimentation in the Nankai Trough as interpreted from magnetic fabric, grain size, and detrital modal analyses. *In* Kagami, H., Karig, D.E., Coulbourn, W.T., et al., *Init. Repts. DSDP,* 87: Washington (U.S. Govt. Printing Office), 611–632.

Underwood, M.B., and Pickering, K.T., 1996. Clay-mineral provenance, sediment dispersal patterns, and mudrock diagenesis in the Nankai accretionary prism, southwest Japan. *Clays Clay Miner.,* 44:339–356.

Underwood, M.B., Orr, R., Pickering, K., and Taira, A., 1993a. Provenance and dispersal patterns of sediments in the turbidite wedge of Nankai Trough. *In* Hill, I.A., Taira, A., Firth, J.V., et al., *Proc. ODP, Sci. Results,* 131: College Station, TX (Ocean Drilling Program), 15–34.

Underwood, M.B., Pickering, K., Gieskes, J.M., Kastner, M., and Orr, R., 1993b. Sediment geochemistry, clay mineralogy, and diagenesis: a synthesis of data from Leg 131, Nankai Trough. *In* Hill, I.A., Taira, A., Firth, J.V., et al., *Proc. ODP, Sci. Results,* 131: College Station, TX (Ocean Drilling Program), 343–363.

Uto, K., and Tatsumi, Y., 1996. Quaternary volcanism of the Japanese Islands. *Isl. Arc,* 5:250–261.

Vrolijk, P., 1990. On the mechanical role of smectite in subduction zones. *Geology,* 18:703–707.

Wang, C.-Y., 1980. Sediment subduction and frictional sliding in a subduction zone. *Geology,* 8:530–533.

Wang, K., Hyndman, R.D., and Yamano, M., 1995. Thermal regime of the southwest Japan subduction zone: effects of age history of the subducting plate. *Tectonophysics,* 248:53–69.

Watanabe, T., 1988. The structural model of illite/smectite interstratified mineral and the diagram for its identificaton. *Clay Sci.,* 7:97–114.

Figure F1. Index map of the Nankai Trough study area (after Shipboard Scientific Party, 2001b). Site 1173 is the reference site for the Muroto Transect, and Site 1177 is the reference site for the Ashizuri Transect. Sites 1174 and 808 (ODP Leg 131) penetrated the frontal décollement of the accretionary prism.

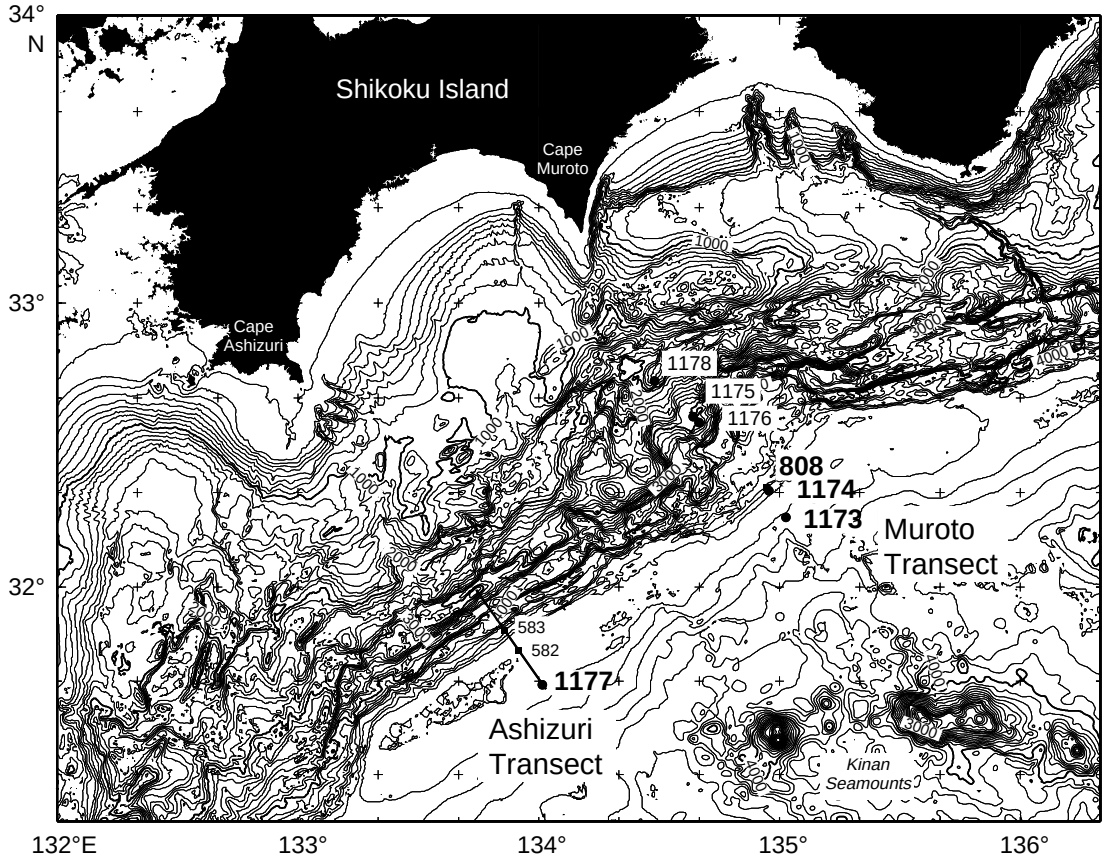

Figure F2. Stratigraphic column for Site 1173 and relative abundances of smectite, illite, chlorite (+ kaolinite), and quartz in the <2-µm fraction. Abundances were calculated using the SVD weighting factors (**Underwood et al.,** this volume) and X-ray diffraction peak areas (Table **T1,** p. 27).

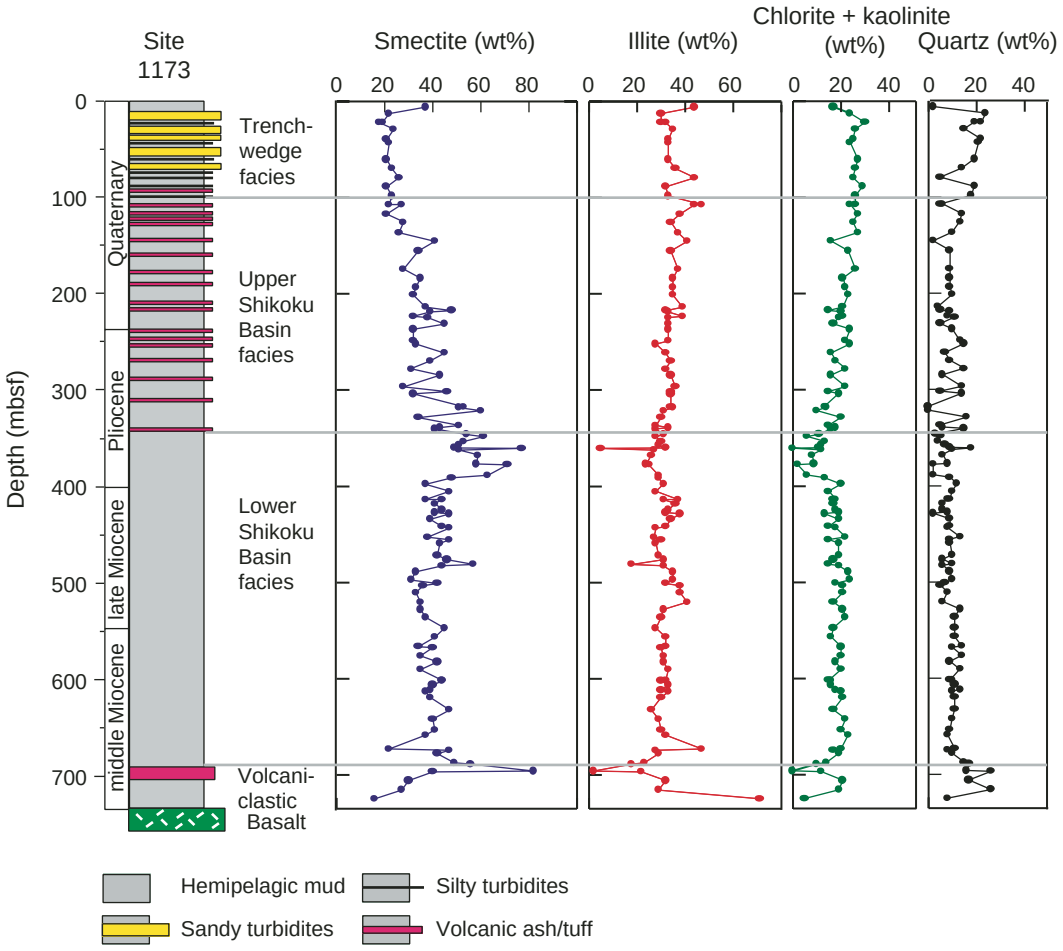

Figure F3. Stratigraphic column for Site 1174 and relative abundances of smectite, illite, chlorite (+ kaolinite), and quartz in the <2-µm fraction. Abundances were calculated using the SVD weighting factors (**Underwood et al.,** this volume) and X-ray diffraction peak areas (Table **T1,** p. 27).

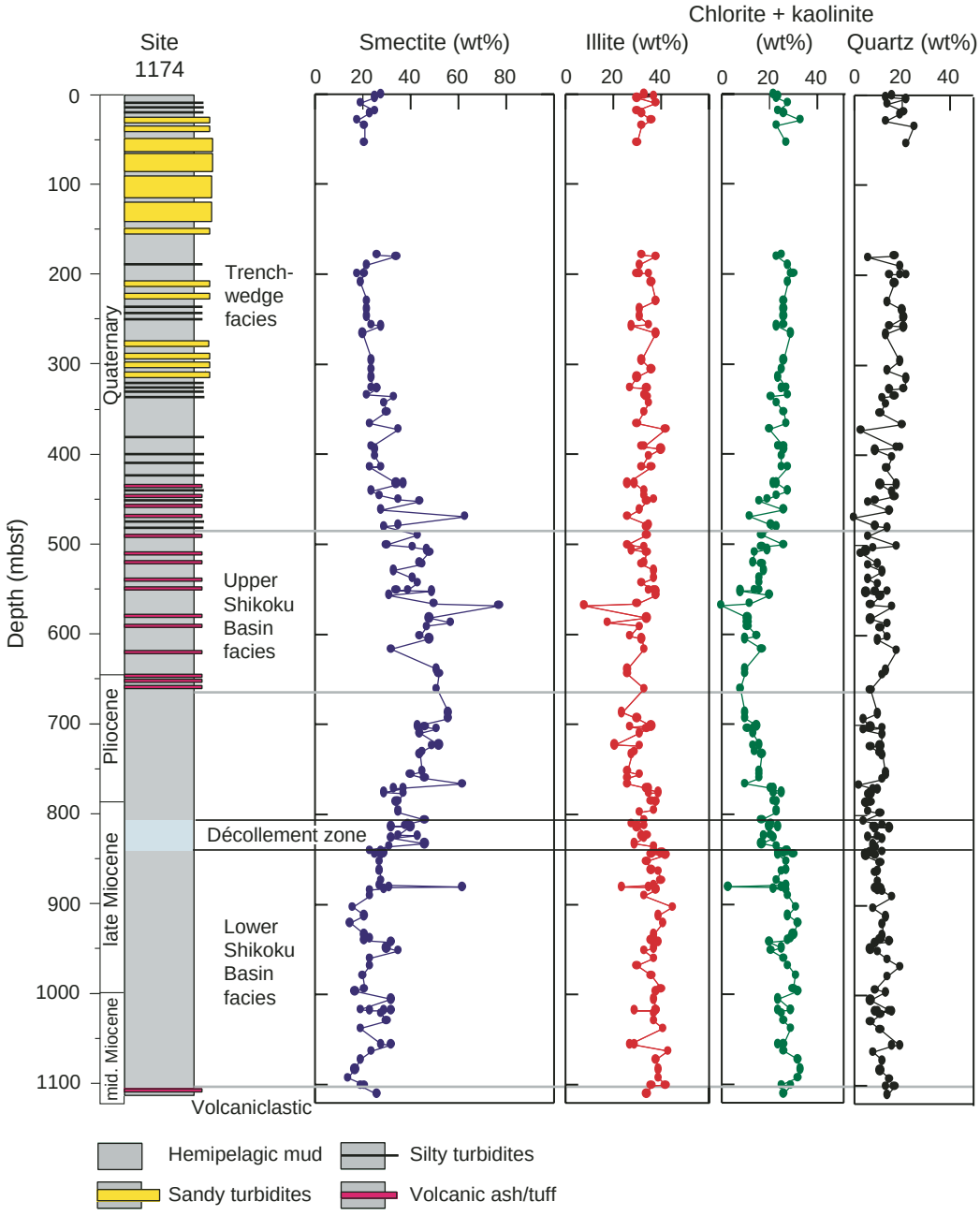

Figure F4. Stratigraphic column and relative abundances of smectite, illite, chlorite (+ kaolinite), and quartz in the <2-µm fraction for Site 1177. Abundances were calculated using the SVD weighting factors (**Underwood et al.,** this volume) and X-ray diffraction peak areas (Table **T1,** p. 27).

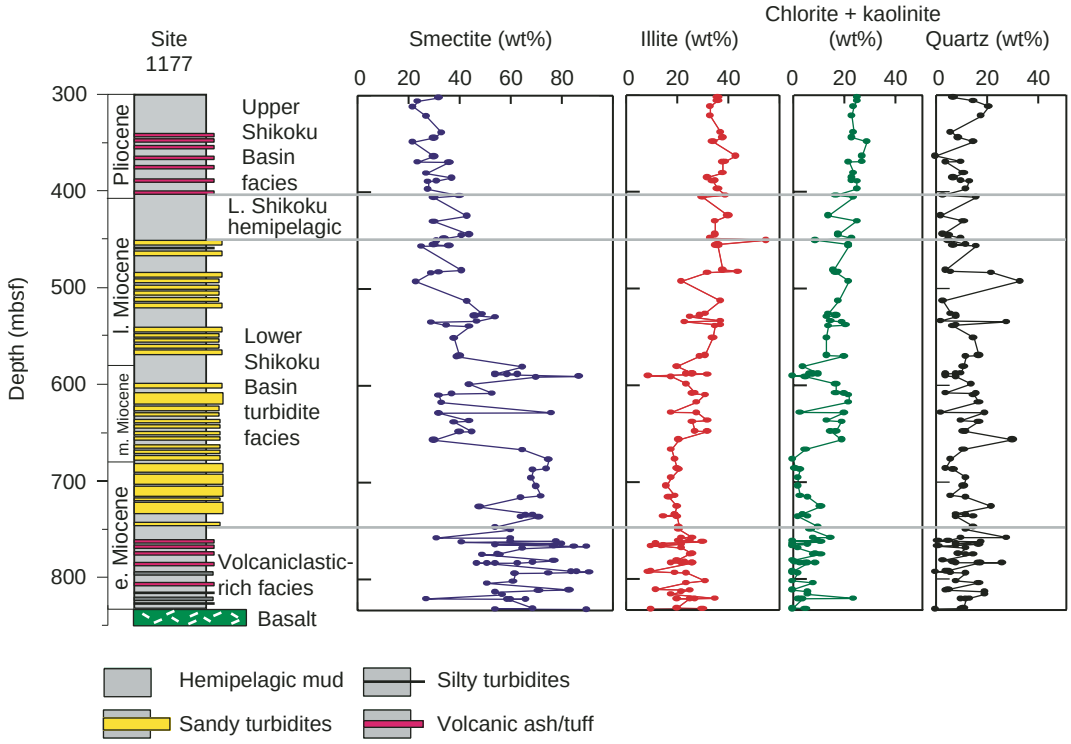

Figure F5. Representative examples of X-ray diffractograms. **A.** Typical result for <2-µm oriented aggregate with identification of major peaks. Ratio of intensity at low angle "saddle" to intensity of 16-Å peak can be used as a measure of expandability (Rettke, 1981). Percent illite in I/S clay also can be calculated using the d-value of I(002)/S(003) reflection (Reynolds and Hower, 1970). * = Used to calculate relative abundance of clay minerals. ** = Used to calculate percent illite in mixed-layer I/S clay. *** = Used to correct peak positions. **B.** Results before and after treatment with HCl to dissolve chlorite. **C.** Display of smectite (060) peak. The d(060) values were corrected using the reference patterns for quartz (112) and quartz (211).

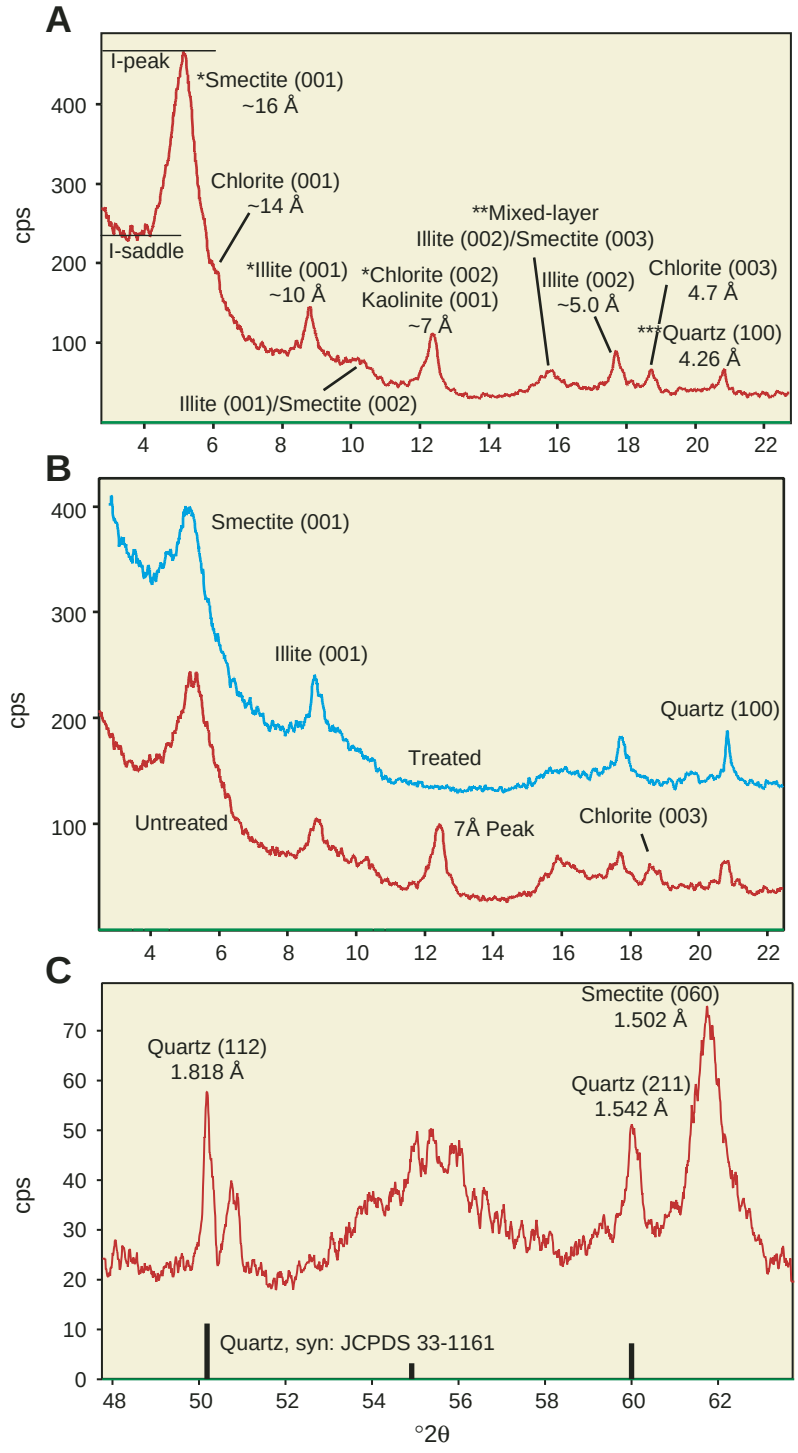

Figure F6. Measured percentages of illite in I/S mixed-layer clays at Sites 808, 1173, 1174, and 1177, based on the d-value of I(002)/S(003) reflections. Solid lines represent numerical simulations of illite–smectite reaction progress using the kinetic model of Huang et al. (1993). Model inputs include paleomagnetic and nannofossil age-depth constraints (Table **T3,** p. 37), potassium concentration from pore water measurements (Shipboard Scientific Party, 1991, 2001c, 2001d, 2001e), and temperature calculated from thermal conductivity data and heat flow (Shipboard Scientific Party, 1991, 2001c, 2001d, 2001e; Fisher et al., 1993). Projected borehole temperatures for Site 1177 were calculated using heat flow from Deep Sea Drilling Project Site 582 (Shipboard Scientific Party, 1986).

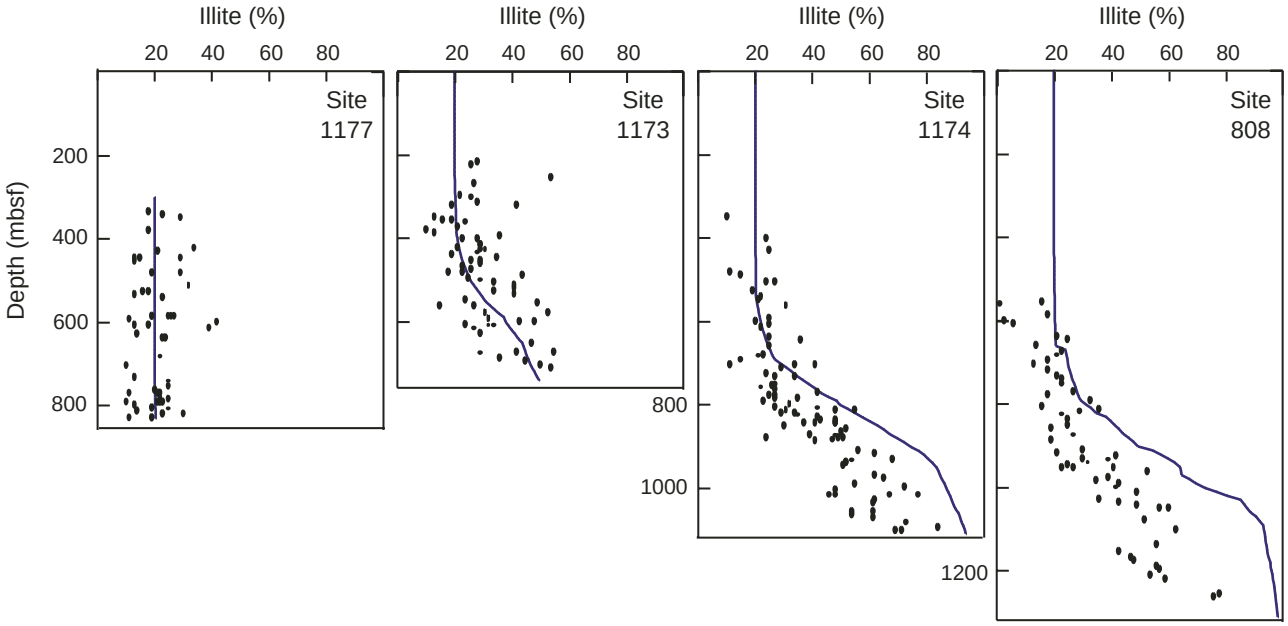

Figure F7. Estimates of absolute abundance of smectite in bulk mudstone, Sites 1173, 1174, and 1177. To compare coeval strata, depths are relative to the top of the Shikoku Basin facies. Estimates were made by multiplying the weight percent total clay minerals (from Shipboard Scientific Party, 2001c, 2001d, 2001e) by the abundance of smectite relative to illite and chlorite (+ kaolinite) in the <2-µm size fraction.

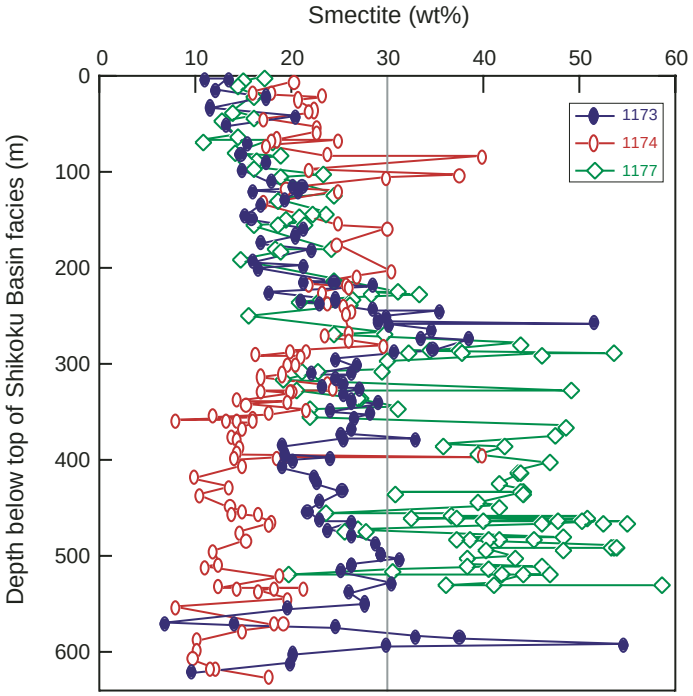

Figure F8. Results of sensitivity analysis for the smectite–illite kinetic model at Sites 1173 and 1174 (see Fig. F6, p. 24). Solid symbols = measured values of percent illite in mixed-layer clay. Variations in heating time were simulated by taking specified percentages (20%, 50%, and 80%) of the actual depositional age at each sample depth (Table T3, p. 37). Linear burial curves are based on total depth at each site divided by maximum age.

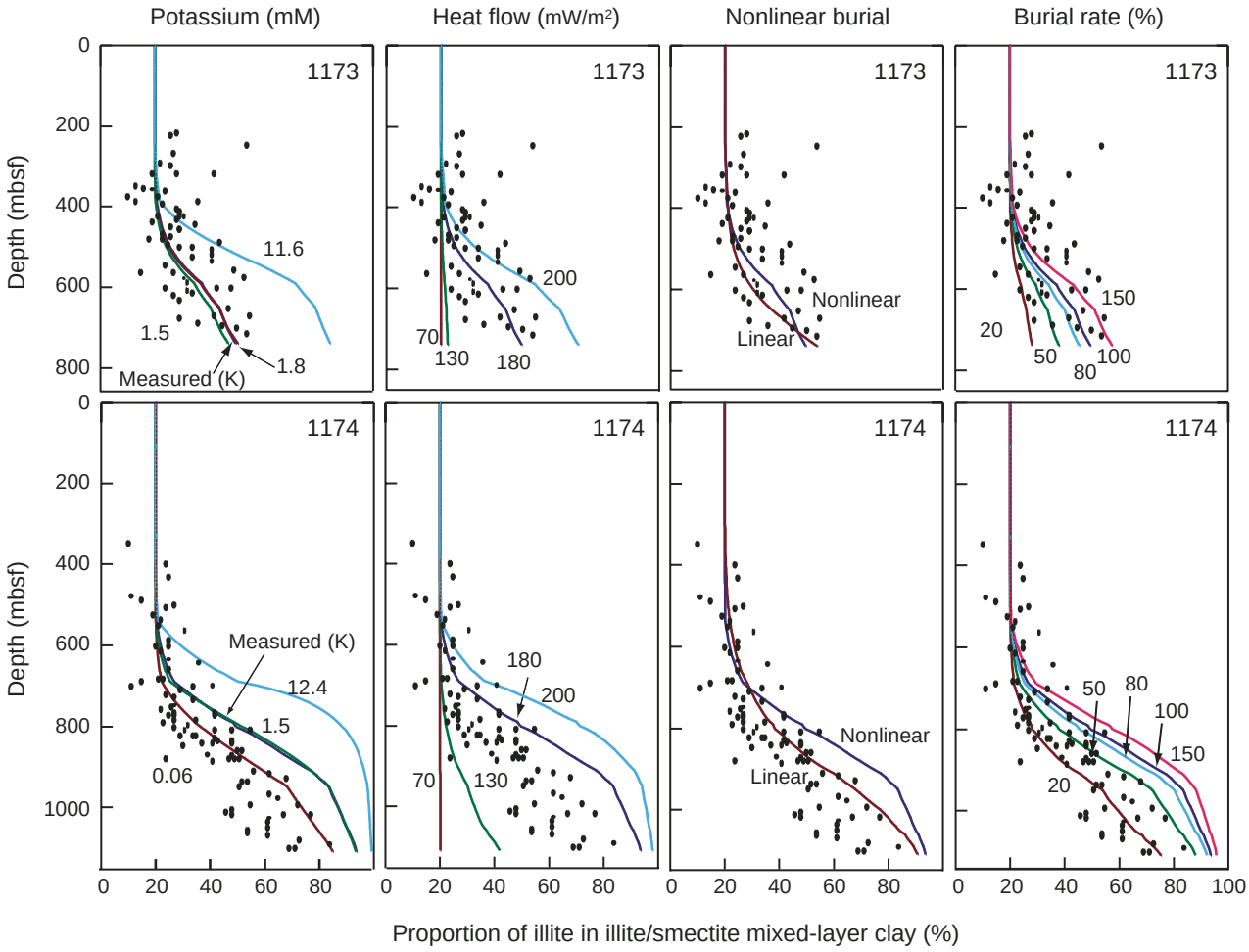

Table T1. Results of X-ray diffraction analysis, <2-µm size fraction, Sites 1173, 1174, and 1177. (See table notes. Continued on next eight pages.)

Core, section, interval (cm)	Depth (mbsf)	XRD peak area (total counts)				Relative mineral abundance: SVD factor (wt%)				Relative mineral abundance: Biscaye factor (area%)			I/S mixed-layer clay			
		Smectite	Illite	Chlorite (+kaolinite)	Quartz	Smectite	Illite	Chlorite (+kaolinite)	Quartz	Smectite	Illite	Chlorite (+kaolinite)	I(002)/S(003) (Å)	Illite in I/S (%)*	I-saddle: I-peak	Expandability (%)†
190-1173A-																
1H-4, 132	6	7,804	4,632	3,810	127	37	44	17	2	23	55	22			0.62	74
2H-4, 136	13	957	1,825	2,245	607	22	30	24	24	8	57	35			0.89	61
3H-4, 126	22	651	1,659	2,760	465	19	30	30	22	5	52	43			0.94	58
3H-4, 126	22	1,396	3,400	5,289	707	18	32	30	19	5	53	41			0.94	58
4H-3, 132	29	2,839	3,057	3,744	460	24	35	26	15	13	54	33			0.84	64
5H-3, 128	40	946	2,473	2,863	615	21	33	25	22	6	60	35			0.91	52
5H-5, 126	43	1,779	2,858	3,360	676	22	33	24	21	9	57	34			0.86	63
7H-4, 128	60	1,508	2,494	3,345	500	21	33	27	19	8	55	37				
8H-4, 133	70	4,775	5,375	6,505	710	23	36	26	14	12	55	33			0.75	68
9H-4, 113	79	8,818	8,235	8,247	294	26	44	25	5	15	57	28			0.79	67
10H-4, 132	89	1,556	2,255	3,396	493	21	32	29	19	9	52	39			0.88	62
11H-4, 107	98	2,335	2,903	3,617	567	23	33	26	18	11	55	34			0.85	64
		Average trench-wedge facies:				23	35	26	17	10	55	35				
12H-4, 48	107	4,973	6,290	6,200	176	22	47	26	5	12	59	29			0.85	64
12H-4, 65	107	10,715	9,863	9,578	398	27	44	24	6	15	57	28			0.75	68
13H-4, 129	117	3,354	5,233	6,106	627	21	38	27	14	9	57	33			0.91	52
14H-3, 131	125	5,092	3,518	4,485	465	28	34	25	13	18	50	32			0.87	63
15H-4, 129	136	6,342	5,075	6,386	478	26	37	27	10	16	52	32			0.85	64
16H-4, 95	146	10,090	4,851	3,970	190	41	41	16	2	27	52	21			0.74	69
17H-4, 133	155	7,088	3,508	4,186	350	34	34	23	9	24	48	28			0.85	64
19H-4, 127	174	8,465	6,368	7,588	535	28	37	26	9	17	52	31			0.82	65
20H-4, 133	184	7,631	3,984	4,271	403	35	35	21	9	24	50	27			0.79	67
21H-4, 106	193	8,792	4,803	5,480	480	33	35	22	9	23	49	28			0.83	65
22H-3, 131	201	5,269	2,972	3,489	304	32	35	23	10	22	49	29			0.84	64
23H-5, 131	214	13,369	6,831	6,940	307	37	39	21	4	24	50	25			0.79	67
24H-1, 123	217	10,371	3,194	3,214	311	48	32	15	5	35	43	22	16	28	0.79	67
24H-2, 128	219	7,600	3,142	3,487	370	39	33	20	9	28	46	26			0.81	66
24H-5, 128	223	9,310	5,860	5,917	429	32	39	21	8	21	53	27			0.81	66
24H-6, 135	225	10,053	4,408	4,571	592	38	33	19	11	27	48	25	15.97	26	0.83	65
25X-4, 125	231	21,079	7,289	7,655	574	45	33	17	5	32	44	23			0.71	70
26X-2, 29	237	6,614	3,471	4,380	398	32	33	24	10	23	47	30			0.88	62
27X-3, 136	249	7,694	4,305	4,951	658	32	33	22	13	22	49	28			0.83	65
27X-5, 110	252	4,624	2,027	2,939	417	33	28	24	15	25	44	32	16.4	54	0.89	61
28X-5, 119	262	15,322	5,202	5,155	543	45	32	16	7	33	45	22			0.75	68
29X-4, 117	270	13,928	5,897	6,082	657	39	34	18	9	28	47	24	15.98	27	0.74	69
30X-3, 112	278	6,842	4,102	4,795	699	31	32	22	15	21	50	29			0.86	63
31X-1, 131	285	13,505	5,112	4,912	469	43	34	16	6	31	47	22			0.76	68
32X-3, 90	297	3,725	2,897	3,021	393	28	36	22	14	17	54	28	15.91	22	0.90	60
32X-6, 130	302	9,140	3,230	2,963	265	46	34	15	5	33	46	21	15.97	26	0.79	67
33X-1, 121	304	4,705	2,827	2,747	444	32	34	19	14	22	53	26			0.86	63
34X-4, 114	318	16,835	4,956	4,551	248	53	34	13	0	37	43	20	16	28	0.93	59
34X-5, 54	318	12,121	3,893	3,556	181	51	35	14	0	35	45	20	16.14	42	0.83	65
34X-CC, 16	322	31,291	7,578	6,759	491	60	31	10	0	42	40	18	15.87	19	0.64	73
35X-5, 102	329	6,416	3,120	3,535	685	34	30	20	16	25	48	27			0.86	63
36X-4, 93	337	16,780	4,265	4,850	473	51	28	15	5	39	39	22			0.66	72

Table T1 (continued).

Core, section, interval (cm)	Depth (mbsf)	XRD peak area (total counts)				Relative mineral abundance: SVD factor (wt%)				Relative mineral abundance: Biscaye factor (area%)			I/S mixed-layer clay			
		Smectite	Illite	Chlorite (+kaolinite)	Quartz	Smectite	Illite	Chlorite (+kaolinite)	Quartz	Smectite	Illite	Chlorite (+kaolinite)	I(002)/S(003) (Å)	Illite in I/S (%)*	I-saddle: I-peak	Expandability (%)†
36X-6, 33	339	5,748	2,074	2,172	188	43	33	18	6	31	45	24			0.86	63
36X-CC, 21	340	6,363	2,150	2,227	481	41	28	16	15	33	44	23			0.86	63
		Average Upper Shikoku Basin facies:				37	35	20	8	26	48	26				
37X-4, 122	346	20,286	5,451	4,794	498	54	31	11	3	39	42	19	15.82	13	0.63	73
37X-6, 35	349	34,783	7,430	5,482	990	61	28	6	5	46	39	15	15.82	13	0.57	76
38X-3, 0	353	23,954	6,340	6,140	583	53	30	13	4	39	41	20			0.62	74
38X-5, 129	358	31,969	8,630	7,981	1,143	51	29	12	7	39	42	19	15.85	16	0.56	76
38X-CC, 21	360	18,934	6,152	4,503	803	49	32	11	9	36	47	17	15.87	19	0.66	72
39X-1, 86	361	50,353	1,079	786	2,746	77	5	0	18	90	8	3			0.27	91
39X-2, 117	363	24,946	6,049	5,855	1,089	51	27	12	10	41	40	19	15.94	24	0.57	76
39X-5, 133	367	22,445	4,632	4,003	705	59	26	8	6	46	38	16			0.57	76
40X-5, 116	377	29,264	5,706	5,250	1,093	58	24	9	8	47	36	17	15.9	21	0.57	76
40X-6, 55	378	55,544	9,627	6,286	1,236	71	25	2	2	52	36	12	15.8	10	0.40	84
41X-7, 26	389	36,667	7,913	6,093	777	63	29	6	2	46	39	15	15.82	13	0.52	78
42X-2, 118	392	22,755	6,589	6,142	983	48	29	13	9	37	43	20	16.08	36	0.57	76
42X-7, 31	398	15,089	6,172	7,235	1,009	37	31	20	12	28	46	27	15.93	23	0.68	71
43X-5, 89	405	17,033	4,828	5,185	782	47	28	15	10	36	41	22	16	28	0.69	71
44X-4, 111	414	12,557	6,560	5,842	646	37	37	18	9	25	52	23	16.02	29	0.74	69
44X-5, 0	414	22,362	7,375	8,034	855	44	31	17	8	33	43	24			0.63	73
44X-CC, 27	418	13,111	5,557	5,314	436	41	36	17	6	29	48	23	16.01	29	0.75	68
45X-5, 121	425	22,210	7,714	8,490	679	44	33	18	6	32	44	24	15.89	21	0.69	71
45X-7, 42	427	13,914	5,127	5,849	598	41	32	19	8	30	44	25	16.02	29	0.71	70
46X-1, 132	429	32,635	12,442	10,268	623	47	38	13	2	32	48	20	16.04	31	0.68	71
46X-5, 121	434	14,477	6,232	6,441	667	39	34	19	9	28	48	25	16	28	0.72	70
4X7-4, 116	442	17,900	6,427	5,966	799	44	32	15	9	32	46	21	15.87	19	0.75	68
47X-5, 130	444	22,515	6,072	7,798	837	47	28	18	8	36	39	25	16.07	35	0.62	74
48X-5, 115	453	12,977	4,344	6,361	920	38	27	22	13	30	40	30	15.97	26	0.72	70
48X-CC, 29	456	21,740	6,500	6,532	927	47	30	15	9	36	43	21	16.02	29	0.69	71
49X-3, 116	459	18,556	5,566	7,186	826	43	28	19	9	34	40	26	16.01	29	0.70	70
50X-5, 118	472	20,711	6,555	8,129	1,024	42	29	19	10	33	41	26	15.92	23	0.67	72
51X-2, 39	476	17,726	5,487	6,014	589	46	31	17	6	34	42	23	15.97	26	0.69	71
51X-5, 118	482	19,267	2,611	4,381	808	57	18	15	10	50	27	23	15.86	18	0.57	76
51X-6, 60	482	16,504	5,425	6,556	519	44	31	19	6	32	42	26	15.93	23	0.74	69
52X-4, 43	489	11,168	6,066	7,075	594	33	35	23	9	23	49	29	16.19	44	0.80	66
53X-3, 90	498	12,933	7,610	9,091	799	31	35	24	10	21	49	30	15.96	25	0.78	67
53X-5, 128	501	19,626	7,062	7,741	725	42	32	18	7	31	45	24	16.01	29	0.69	71
53X-CC, 26	503	19,019	9,651	10,179	592	36	38	21	5	24	50	26	16.06	34	0.77	68
54X-5, 119	511	15,286	9,065	9,126	757	33	38	21	8	22	52	26	16.12	41	0.82	65
55X-5, 131	520	13,774	8,273	6,864	490	35	41	17	6	23	55	23	16.12	41	0.76	68
56X-4, 112	528	11,484	5,429	6,305	907	35	31	21	13	25	47	28	16.06	34	0.79	67
57X-3, 113	536	15,914	6,074	8,292	888	37	30	22	11	28	43	29	16.12	41	0.73	69
58X-4, 118	547	21,381	6,237	7,105	1,074	45	28	17	11	35	41	23	15.95	24	0.68	71
59X-4, 115	557	13,824	5,324	4,974	808	41	32	16	11	31	47	22	16.28	49	0.71	70
60X-4, 115	567	11,389	5,883	6,398	1,029	34	32	20	14	24	49	27	15.84	15	0.72	70
60X-5, 82	568	16,733	5,858	7,238	837	40	30	20	10	31	43	26	15.98	27	0.72	70
61X-4, 116	576	7,998	3,672	4,240	636	35	31	20	14	26	47	27	16.38	53	0.74	69

Table T1 (continued).

Core, section, interval (cm)	Depth (mbsf)	XRD peak area (total counts)				Relative mineral abundance: SVD factor (wt%)				Relative mineral abundance: Biscaye factor (area%)			I/S mixed-layer clay			
		Smectite	Illite	Chlorite (+kaolinite)	Quartz	Smectite	Illite	Chlorite (+kaolinite)	Quartz	Smectite	Illite	Chlorite (+kaolinite)	I(002)/S(003) (Å)	Illite in I/S (%)*	I-saddle: I-peak	Expandability (%)†
62X-2, 52	582	24,624	8,709	9,365	1,068	42	31	18	9	31	45	24	16.04	31	0.70	70
63X-1, 83	591	13,554	6,754	7,255	1,010	35	33	20	13	25	49	26	16.05	32	0.73	69
64X-2, 99	602	16,428	5,862	5,274	783	44	32	15	9	33	47	21	16.16	43	0.69	71
64X-2, 120	602	20,952	6,920	7,258	994	44	30	16	10	33	44	23	16.25	48	0.65	73
64X-5, 56	606	15,339	6,569	5,815	905	40	33	16	11	29	49	22	15.94	24	0.70	70
65X-2, 105	612	14,720	5,691	6,031	994	39	30	18	13	30	46	24	16.05	32	0.71	70
65X-3, 109	613	16,666	7,399	8,247	910	37	33	20	10	27	47	26	16.06	34	0.73	69
66X-1, 60	619	9,817	3,628	4,604	551	39	30	21	11	29	43	27	15.98	27	0.77	68
67X-3, 90	632	17,541	4,437	5,470	883	47	26	17	11	38	38	24	16.02	29	0.70	70
68X-3, 67	642	16,166	5,374	7,424	788	40	29	22	10	31	41	28			0.70	70
69X-4, 89	653	17,260	5,824	7,161	811	41	30	20	9	31	42	26	16.24	47	0.73	69
70X-1, 112	659	13,780	5,510	7,421	579	37	32	23	8	27	44	29			0.79	67
71X-4, 119	673	1,501	2,678	1,961	200	22	47	20	11	9	66	24	16.44	55	0.94	58
71X-5, 130	674	18,006	5,038	5,850	735	47	28	17	8	36	40	23	16.14	42	0.72	70
72X-1, 126	678	19,334	6,242	7,848	959	42	29	19	10	32	42	26	16.02	29	0.69	71
73X-1, 117	688	14,552	3,044	3,531	956	49	23	14	15	43	36	21			0.61	74
		Average Lower Shikoku Basin facies:				44	30	17	9	33	43	23				
73X-2, 86	689	21,224	2,828	3,057	1,431	56	18	10	17	55	29	16	16.08	36	0.55	77
74X-1, 10	696	62,556	381	523	3,062	82	2	0	16	96	2	2			0.13	100
74X-CC, 21	697	9,921	2,779	2,057	1,666	40	22	12	26	39	44	16	16.2	45	0.74	69
75X-CC, 20	706	8,818	5,573	6,257	1,121	30	32	21	17	20	51	29	16.3	50	0.88	62
76X-CC, 15	715	2,586	2,787	2,530	1,060	27	29	19	26	14	59	27	16.42	54	0.93	59
77X-CC, 14	725	512	12,381	2,625	363	16	71	5	8	1	90	9				
			Average volcaniclastic facies:			42	29	11	18	38	46	16				
190-1174B-																
1R-1, 137	1	3,611	2,824	3,141	512	28	33	22	16	17	53	30			0.88	62
1R-2, 94	2	5,513	5,566	6,059	667	25	37	24	13	14	56	30			0.78	67
1R-3, 106	4	2,004	2,091	2,596	606	25	30	23	22	13	54	33			0.86	63
2R-5, 132	11	2,060	4,026	4,767	474	19	38	28	14	7	58	34			0.84	64
3R-4, 77	19	2,036	1,980	2,602	538	25	30	24	21	13	52	34			0.86	63
3R-6, 86	21	2,605	3,325	4,382	756	23	32	26	19	11	54	36			0.90	60
4R-4, 127	29	1,889	2,914	4,641	311	18	36	33	13	8	51	41			0.91	60
5R-2, 131	36	320	1,471	1,521	444	21	32	23	25	3	64	33			0.88	62
7R-2, 127	54	839	1,620	2,299	469	21	30	27	22	7	54	39				
5R-1, 36	179	3,466	2,910	3,796	549	26	32	25	17	15	51	33			0.85	64
5R-1, 122	180	8,221	4,596	5,088	268	34	38	23	6	22	50	28			0.71	70
6R-1, 117	190	2,731	3,393	5,113	793	22	31	28	19	10	51	39			0.81	66
7R-1, 93	199	648	2,272	3,923	635	18	30	30	22	4	52	45			0.85	64
7R-1, 93	199	2,124	2,977	4,687	660	21	31	29	19	9	51	40			0.85	64
7R-1, 93	199	2,763	3,685	5,162	526	21	35	29	15	10	53	37			0.85	64
8R-1, 58	209	1,639	3,686	4,675	547	19	36	28	17	6	57	36			0.90	60
10R-CC, 16	229	2,376	3,075	3,573	368	22	38	26	14	11	56	33			0.91	60
11R-2, 17	238	1,767	2,643	3,615	641	22	31	26	20	9	54	37			0.80	66
12R-1, 108	248	1,388	2,283	3,107	598	22	31	26	21	8	55	37			0.96	54
13R-1, 20	256	3,591	3,716	4,558	566	24	35	26	15	13	54	33			0.87	63
13R-1, 107	257	3,089	1,995	2,758	636	28	28	23	21	19	48	33			0.82	65

Table T1 (continued).

Core, section, interval (cm)	Depth (mbsf)	XRD peak area (total counts)				Relative mineral abundance: SVD factor (wt%)				Relative mineral abundance: Biscaye factor (area%)			I/S mixed-layer clay			
		Smectite	Illite	Chlorite (+kaolinite)	Quartz	Smectite	Illite	Chlorite (+kaolinite)	Quartz	Smectite	Illite	Chlorite (+kaolinite)	I(002)/S(003) (Å)	Illite in I/S (%)*	I-saddle: I-peak	Expandability (%)†
14R-1, 16	266	4,465	6,543	8,473	674	20	38	29	13	9	55	36			0.73	69
17R-1, 108	296	2,125	2,219	2,955	479	24	32	26	19	13	52	35			0.88	62
18R-2, 63	306	4,023	4,200	4,878	541	24	36	25	14	13	55	32			0.85	64
19R-1, 73	315	2,319	2,588	3,353	740	24	30	24	22	12	53	35			0.85	64
20R-2, 109	326	2,687	2,280	3,907	722	24	27	27	21	14	46	40			0.85	64
20R-CC, 13	327	5,753	5,089	6,130	798	26	34	25	15	15	53	32			0.87	63
21R-1, 122	334	2,778	3,332	4,638	629	22	33	28	17	11	53	37			0.88	62
21R-CC, 5	336	4,245	2,392	2,598	308	33	34	21	12	22	50	27			0.90	60
22R-1, 22	343	6,823	4,669	5,236	650	29	35	23	13	19	52	29			0.84	64
23R-1, 94	353	12,433	7,039	9,523	830	30	33	26	11	21	47	32	15.8	10	0.78	67
24R-3, 118	366	1,328	1,460	2,153	377	23	30	27	20	12	51	38			0.92	59
25R-1, 122	373	11,797	6,992	6,448	227	35	42	20	3	22	53	24			0.68	71
27R-1, 119	392	3,323	3,551	4,660	707	24	33	26	18	12	53	35			0.83	65
27R-1, 119	392	3,856	4,098	5,005	909	24	32	24	19	13	54	33			0.83	65
27R-3, 113	395	5,159	4,719	5,403	335	25	40	26	9	15	54	31			0.87	63
28R-2, 50	402	4,043	4,004	4,691	657	25	35	25	16	14	54	32	15.93	23	0.86	63
29R-3, 128	414	7,389	4,931	6,616	804	28	32	25	14	18	49	33			0.80	66
29R-CC, 20	415	2,718	2,914	3,841	354	23	36	28	13	12	53	35			0.86	63
31R-3, 47	432	9,382	3,740	5,436	1,118	34	26	22	18	27	42	31	15.96	25	0.72	70
31R-3, 49	432	14,320	5,366	7,828	857	37	29	23	11	28	42	30			0.74	69
32R-2, 118	441	4,251	4,130	5,878	722	24	33	28	16	13	51	36			0.89	61
32R-5, 127	446	2,443	1,996	2,299	396	27	33	23	17	16	53	31			0.94	58
33R-2, 116	451	13,155	7,188	6,872	707	35	37	19	9	24	52	25			0.70	70
33R-4, 15	453	13,176	5,017	4,640	458	44	34	16	6	31	47	22			0.73	69
34R-3, 99	462	5,540	3,473	5,061	618	28	31	26	15	19	47	34			0.85	64
35R-2, 94	470	12,058	2,295	2,672	175	63	26	12	0	45	35	20			0.68	71
36R-2, 130	479	13,251	6,664	7,251	634	35	35	21	9	24	49	27	15.81	11	0.69	71
36R-3, 108	481	6,203	4,499	5,052	663	29	34	23	14	18	52	29			0.84	64
		Average trench-wedge facies:				27	33	25	15	15	52	33				
37R-3, 133	490	14,125	5,347	5,447	441	43	34	17	6	30	46	23	15.84	15	0.68	71
38R-4, 113	501	5,302	2,466	4,463	720	30	26	26	18	22	41	37			0.78	67
38R-6, 60	503	12,176	4,700	4,759	517	41	33	17	8	30	46	24	15.98	27	0.73	69
39R-1, 127	506	22,831	6,241	8,248	659	47	28	19	5	36	39	26	15.94	24	0.62	74
39R-3, 115	509	11,588	3,889	3,596	274	48	34	14	3	34	45	21			0.69	71
40R-4, 115	520	10,884	3,994	3,257	537	44	33	13	10	33	48	20			0.78	67
40R-5, 135	522	12,343	4,232	4,347	415	45	32	17	6	33	45	23			0.74	69
41R-CC, 23	529	10,907	6,726	5,996	796	33	37	18	12	22	54	24	15.87	19	0.75	68
42R-3, 127	538	19,248	8,291	7,525	637	41	37	16	6	29	49	22			0.64	73
42R-CC, 9	544	18,219	6,617	6,377	892	43	32	16	10	32	46	22	15.91	22	0.77	68
43R-5, 123	551	10,482	5,206	3,843	548	39	37	14	9	27	53	20	15.9	21	0.76	68
43R-5, 148	551	10,011	5,901	4,592	918	34	35	16	14	23	55	21	15.9	21	0.80	66
43R-6, 127	552	23,007	8,604	5,214	692	49	38	8	5	34	51	15			0.64	73
44R-3, 115	557	7,388	4,990	4,746	506	31	38	20	11	20	54	26			0.80	66
45R-3, 111	567	20,139	5,698	5,135	733	50	30	12	7	38	43	19	16.04	31	0.64	73
45R-CC, 7	568	57,980	2,379	1,787	2,930	77	8	0	16	82	13	5			0.26	91
46R-7, 39	582	15,952	5,429	3,976	610	48	34	11	7	35	48	17			0.65	73

Table T1 (continued).

Core, section, interval (cm)	Depth (mbsf)	XRD peak area (total counts)				Relative mineral abundance: SVD factor (wt%)				Relative mineral abundance: Biscaye factor (area%)			I/S mixed-layer clay			
		Smectite	Illite	Chlorite (+kaolinite)	Quartz	Smectite	Illite	Chlorite (+kaolinite)	Quartz	Smectite	Illite	Chlorite (+kaolinite)	I(002)/S(003) (Å)	Illite in I/S (%)*	I-saddle: I-peak	Expandability (%)†
47R-4, 118	588	17,596	2,429	3,086	944	57	18	11	14	53	29	18			0.53	78
47R-CC, 0	591	17,830	5,803	4,427	941	47	31	11	11	36	47	18	15.95	25	0.64	73
49R-1, 117	602	12,735	3,660	3,801	873	44	27	15	14	36	42	22	15.88	20	0.68	71
49R-3, 97	605	14,729	4,789	3,413	717	48	32	10	10	36	47	17	15.95	25	0.63	73
50R-4, 117	617	6,346	4,249	3,424	902	32	33	17	18	21	56	23	15.91	22	0.79	67
52R-6, 113	639	16,421	4,061	3,197	936	51	26	10	13	42	42	16	15.95	25	0.64	73
53R-3, 124	644	13,524	3,163	2,659	713	52	26	10	12	43	40	17	16.08	36	0.65	73
55R-1, 129	660	11,000	3,484	2,247	413	51	33	8	7	37	47	15	15.96	25	0.74	69
		Average Upper Shikoku Basin facies:				45	31	14	10	34	45	20				
57R-6, 135	687	13,752	2,724	2,590	595	56	24	10	10	46	37	17	15.9	21	0.62	74
58R-4, 82	693	38,740	9,587	8,435	983	56	30	10	4	41	41	18	15.84	15	0.49	80
59R-3, 118	702	24,283	9,992	8,431	893	43	36	15	7	30	49	21	16.12	41	0.70	70
59R-4, 86	703	21,592	5,934	6,083	1,248	46	27	14	12	38	41	21	15.81	11	0.64	73
59R-5, 133	705	17,453	5,574	4,359	475	51	34	11	4	36	46	18	16.06	34	0.66	72
60R-2, 111	710	22,384	7,991	6,584	1,290	44	31	13	12	33	47	20	16.02	29	0.63	73
61R-4, 107	722	23,302	4,196	6,066	1,100	52	21	16	11	45	32	23			0.54	77
61R-5, 117	724	31,492	9,529	8,728	1,126	49	31	13	7	36	44	20	15.94	24	0.61	74
62R-3, 92	730	18,402	5,854	5,479	1,015	45	29	14	11	35	44	21	15.99	27	0.58	75
62R-CC, 0	734	19,899	5,958	6,719	1,144	44	28	17	12	35	42	24	16.06	34	0.63	73
64R-5, 108	753	20,339	5,519	6,459	1,236	45	26	16	13	37	40	23	15.98	27	0.58	75
65R-1, 118	756	11,253	4,543	4,234	779	40	31	16	13	30	48	22	15.97	26	0.70	70
65R-4, 78	760	26,896	7,162	8,192	1,516	46	26	16	12	37	40	23	15.91	22	0.56	76
66R-1, 118	766	54,693	10,821	10,752	1,170	62	26	10	2	46	36	18	15.99	27	0.45	81
66R-5, 82	771	15,333	8,376	9,321	896	33	35	22	10	23	50	28	16.15	42	0.73	69
66R-5, 104	772	15,562	6,901	7,987	650	37	34	21	8	26	47	27	16.15	42	0.71	70
67R-2, 96	775	10,125	7,209	8,277	435	29	39	25	7	18	52	30	15.98	27	0.77	68
67R-3, 126	777	17,309	7,811	9,006	609	37	35	22	6	26	47	27	15.95	25	0.72	70
68R-1, 116	785	21,915	11,235	12,735	870	35	36	22	7	24	49	28	16.07	35	0.70	70
68R-2, 134	787	17,094	9,415	10,291	505	34	38	23	5	23	50	27	15.99	27	0.73	69
69R-2, 127	795	12,676	6,508	7,556	420	35	37	23	6	24	48	28	15.92	23	0.74	69
69R-4, 119	798	9,913	4,415	5,738	628	35	31	23	11	25	45	29	16.05	32	0.77	68
70R-2, 94	806	26,838	8,839	9,616	643	46	33	17	4	33	43	24	15.99	27	0.59	75
70R-CC, 0	811	13,474	4,598	6,263	857	39	28	21	12	30	41	28	16.14	42	0.73	69
71R-2, 1	813	11,231	4,653	5,327	497	38	33	20	8	28	46	26	16.04	31	0.79	67
71R-2, 65	814	9,424	4,658	6,386	885	32	30	24	15	23	46	31	16.25	48	0.80	66
71R-2, 94	814	18,077	6,476	7,878	868	40	30	20	9	30	43	26	16.43	55	0.69	71
72R-1, 42	823	14,251	6,805	7,859	776	35	34	21	10	25	48	27	16.06	34	0.79	67
72R-1, 117	823	12,390	4,392	4,883	414	43	32	18	6	31	44	25	16.01	29	0.67	72
72R-3, 100	826	11,482	6,322	7,395	839	32	33	22	12	22	49	29	16.07	35	0.75	68
73R-1, 80	833	18,405	5,355	6,161	741	46	29	17	8	35	41	24	16.15	42	0.65	73
73R-3, 116	836	8,533	5,445	6,099	469	31	37	23	9	20	51	29	16.17	43	0.81	66
73R-5, 111	839	5,031	5,406	6,679	576	23	37	27	12	13	54	33	16.25	48	0.87	63
73R-7, 51	841	7,383	4,926	6,622	305	28	37	28	7	18	49	33	16.12	41	0.84	64
74R-1, 130	843	9,451	7,012	7,444	305	29	41	24	5	18	54	28	16.26	48	0.86	63
74R-2, 58	843	9,367	6,575	7,680	298	29	40	26	5	18	52	30	16.25	48	0.85	64
74R-2, 125	844	7,313	5,637	8,051	455	25	36	30	9	16	49	35			0.86	63

Table T1 (continued).

Core, section, interval (cm)	Depth (mbsf)	XRD peak area (total counts)				Relative mineral abundance: SVD factor (wt%)				Relative mineral abundance: Biscaye factor (area%)			I/S mixed-layer clay			
		Smectite	Illite	Chlorite (+kaolinite)	Quartz	Smectite	Illite	Chlorite (+kaolinite)	Quartz	Smectite	Illite	Chlorite (+kaolinite)	I(002)/S(003) (Å)	Illite in I/S (%)*	I-saddle: I-peak	Expandability (%)†
74R-CC, 14	845	13,217	10,602	11,082	429	28	42	24	5	17	55	28	16.09	37	0.80	66
75R-1, 97	852	8,278	5,860	8,025	655	27	34	27	11	17	49	34	16.03	30	0.83	65
76R-1, 73	861	9,850	7,341	9,556	692	27	36	27	10	17	50	33	16.36	52	0.82	65
76R-2, 81	863	10,754	8,599	9,628	695	27	39	25	9	17	53	30	16.29	50	0.81	66
77R-2, 91	873	11,504	9,650	9,605	801	28	40	23	10	17	56	28	16.1	39	0.88	62
77R-6, 44	878	11,700	8,668	10,921	759	27	37	27	10	17	51	32	16.25	48	0.85	64
78R-1, 55	881	27,669	5,072	2,516	1,276	62	24	3	11	52	38	9	15.94	24	0.59	75
78R-1, 95	881	14,430	8,183	10,390	741	31	35	25	9	21	48	31	16.27	49	0.84	64
78R-2, 128	883	5,540	4,016	4,148	372	29	38	22	10	19	54	28	16.33	51	0.88	62
78R-3, 96	884	6,207	6,659	7,988	676	23	38	27	12	13	55	33	16.23	47	0.89	61
79R-1, 118	890	4,351	4,641	6,467	768	23	33	28	16	12	52	36	16.13	41	0.91	60
80R-3, 113	903	2,794	6,237	7,360	254	16	45	31	8	7	59	35			0.91	60
81R-3, 102	913	4,642	6,610	7,883	656	21	39	28	13	10	56	34	16.49	56	0.91	60
82R-2, 92	921	1,269	4,531	5,901	371	15	41	32	12	4	58	38	16.64	62	0.93	59
83R-4, 112	934	4,669	6,032	8,060	592	21	37	30	12	10	54	36	16.75	68	0.87	63
83R-7, 46	937	5,246	5,128	6,805	508	23	37	29	11	13	52	35	16.4	54	0.87	63
84R-2, 117	940	3,426	4,888	6,290	668	21	36	28	15	10	55	35	16.36	52	0.92	59
84R-3, 132	942	6,825	4,343	4,180	358	32	39	20	9	21	53	26	16.36	52	0.83	65
85R-1, 117	948	10,680	6,579	8,040	454	30	37	25	7	20	50	30	16.33	51	0.85	64
85R-3, 116	951	9,466	4,435	5,141	527	35	33	21	10	25	47	27			0.76	68
86R-2, 117	959	6,287	7,292	8,656	878	23	37	26	14	12	55	33			0.90	60
87R-1, 127	968	2,217	2,508	3,892	611	23	30	28	19	11	50	39	16.63	62	0.88	62
88R-2, 114	979	4,628	6,652	9,503	786	20	36	31	14	9	53	38	16.69	65	0.94	58
89R-6, 31	993	5,538	7,180	8,955	468	21	40	30	9	11	55	34	16.44	55	0.89	61
90R-2, 5	996	2,438	5,737	8,175	563	17	38	32	13	6	55	39	16.84	72	0.87	63
91R-1, 88	1,005	13,948	8,149	9,660	593	32	37	24	7	21	49	29	16.25	48	0.81	66
92R-2, 67	1,016	3,506	7,032	8,760	838	19	38	29	15	7	57	36	16.22	46	0.89	61
92R-3, 87	1,018	6,017	6,180	8,109	505	23	38	29	10	13	53	35	16.98	77	0.87	63
92R-3, 94	1,018	8,179	4,004	5,657	857	32	29	24	16	23	45	32	16.25	48	0.80	66
92R-3, 94	1,018	11,186	7,862	8,802	686	29	38	24	9	19	52	29	16.74	67	0.80	66
92R-5, 89	1,021	10,047	7,672	9,022	794	28	37	25	11	17	52	31			0.85	64
93R-4, 114	1,030	14,073	8,724	10,766	568	30	37	26	7	20	49	31	16.63	62	0.81	66
94R-3, 131	1,038	2,721	5,202	6,128	403	19	41	29	11	8	58	34	16.61	61	0.94	58
96R-2, 116	1,055	3,955	2,265	3,739	645	28	27	26	19	19	44	36	16.61	61	0.85	64
96R-3, 17	1,056	8,604	4,086	5,927	896	32	29	24	16	23	44	32	16.42	54	0.81	66
97R-1, 63	1,063	6,329	6,667	7,045	357	24	43	26	8	13	57	30	16.41	54	0.87	63
98R-1, 28	1,072	3,592	5,503	7,839	496	19	38	32	12	9	53	38	16.61	61	0.85	64
99R-2, 26	1,083	3,062	6,436	9,236	486	17	39	33	11	6	54	39	16.86	73	0.93	59
100R-1, 100	1,092	736	6,164	8,183	708	14	39	32	15	2	59	39	17.37	89	0.95	55
101R-1, 13	1,101	4,142	7,343	7,147	712	21	42	25	13	9	61	30	16.82	71	0.93	59
101R-1, 54	1,101	1,858	4,176	5,506	653	19	36	29	17	6	56	37	16.78	69	0.90	60
		Average Lower Shikoku Basin facies:				32	35	23	10	21	49	29				
102R-1, 66	1,111	5,431	4,418	5,708	620	26	34	26	14	16	51	33			1	60
190-1177A-																
1R-2, 82	303	11,738	6,500	7,907	443	32	36	25	7	22	49	30			0.74	69
1R-4, 128	306	2,003	2,215	2,556	309	24	36	25	15	13	55	32			0.92	59

Table T1 (continued).

Core, section, interval (cm)	Depth (mbsf)	XRD peak area (total counts)				Relative mineral abundance: SVD factor (wt%)				Relative mineral abundance: Biscaye factor (area%)			I/S mixed-layer clay			
		Smectite	Illite	Chlorite (+kaolinite)	Quartz	Smectite	Illite	Chlorite (+kaolinite)	Quartz	Smectite	Illite	Chlorite (+kaolinite)	I(002)/S(003) (Å)	Illite in I/S (%)*	I-saddle: I-peak	Expandability (%)†
2R-2, 111	312	2,385	3,717	4,318	868	22	33	24	21	9	57	33			0.92	59
3R-2, 124	322	5,935	5,099	5,768	1,017	27	33	23	18	16	54	30			0.87	63
5R-1, 36	338	6,897	3,799	4,495	219	33	37	24	6	22	49	29	15.86	18	0.78	67
5R-5, 123	344	8,358	5,648	6,046	500	30	38	23	9	19	52	28	15.93	23	0.85	64
6R-1, 68	348	3,000	3,265	4,647	487	22	34	29	15	12	52	37	16.02	29	0.90	60
7R-4, 120	363	7,269	4,797	5,639	0	30	43	27	0	19	51	30			0.89	61
8R-2, 30	369	4,738	4,765	5,729	371	24	39	27	10	13	54	32			0.90	60
8R-2, 53	369	12,064	6,073	6,601	274	36	38	22	4	24	49	27			0.84	64
9R-3, 108	381	7,322	6,353	6,741	612	27	38	24	11	16	55	29	15.86	18	0.91	60
9R-CC, 6	385	15,091	6,166	8,070	565	37	32	23	7	27	44	29			0.75	68
10R-2, 118	389	10,610	6,330	7,213	681	31	35	23	10	21	50	29			0.85	64
10R-2, 148	389	5,515	3,801	4,787	512	28	34	25	13	18	50	32			0.90	60
11R-1, 134	397	3,955	2,945	3,502	344	28	36	25	12	17	52	31			0.85	64
		Average Upper Shikoku Basin facies:				29	36	25	10	18	52	30				
11R-CC, 10	404	17,452	8,161	7,386	374	40	39	17	3	27	50	23			0.79	67
12R-1, 44	406	3,326	1,840	2,484	390	30	30	24	16	21	47	32			0.92	59
13R-CC, 27	425	22,487	10,174	8,116	469	43	40	14	2	28	51	20	16.06	34	0.77	68
14R-4, 127	430	7,724	4,918	6,041	521	30	35	25	11	20	50	31	15.9	21	0.81	66
15R-CC, 8	444	11,882	4,366	4,502	272	44	35	18	3	31	46	23	15.84	15	0.80	66
16R-1, 89	445	16,325	6,564	6,777	465	41	35	18	5	29	47	24			0.83	65
16R-3, 119	448	13,473	6,522	7,991	747	34	33	23	10	24	47	29	15.82	13	0.77	68
		Average Lower Shikoku hemipelagic facies:				38	35	20	7	26	48	26				
16R-4, 144	450	12,996	14,392	6,043	512	31	55	9	5	16	70	15	16.01	29	0.88	62
17R-1, 118	455	9,260	6,163	6,485	784	30	36	22	12	20	53	28	15.82	13	0.83	65
17R-2, 26	455	19,653	9,261	10,626	803	36	35	22	7	25	48	27			0.76	68
17R-2, 99	456	3,444	3,913	3,854	618	25	36	22	16	13	58	29			0.93	59
19R-6, 42	481	20,925	9,199	8,196	584	41	38	16	4	28	50	22	15.87	19	0.78	67
19R-7, 36	482	13,817	10,577	8,155	579	32	44	18	6	19	58	23	16.01	29	0.84	64
20R-1, 104	483	5,377	4,497	3,400	1,259	29	32	17	22	18	60	23			0.85	64
21R-1, 34	492	0	1,390	2,092	1,304	23	22	22	33	0	57	43				
23R-2, 42	513	13,021	5,223	5,213	268	43	37	18	3	29	47	24	16.05	32	0.75	68
24R-4, 56	526	14,806	4,318	4,314	456	49	31	14	6	36	42	21	15.85	16	0.77	68
24R-5, 128	528	17,423	5,175	5,914	708	46	29	17	8	35	41	24	15.86	18	0.69	71
24-6, 127	529	15,728	3,367	3,759	595	54	25	13	8	43	37	20			0.58	75
25R-2, 130	533	27,598	10,384	9,164	495	47	37	15	2	32	47	21	15.82	13	0.69	71
25R-3, 85	534	4,409	2,607	3,098	1,632	29	23	19	28	21	50	29			0.87	63
25R-5, 121	538	14,432	7,669	7,945	655	35	37	21	8	24	50	26			0.79	67
25R-6, 105	539	18,243	6,965	5,898	693	44	35	14	7	32	48	20	15.92	23	0.74	69
27R-1, 97	551	10,268	5,140	3,430	898	38	34	13	15	27	55	18			0.81	66
29R-1, 34	569	9,211	3,860	2,678	898	40	31	13	17	31	51	18			0.86	63
29R-1, 85	570	14,076	4,967	6,235	829	39	29	20	12	30	43	27			0.73	69
30R-2, 30	580	25,477	3,556	2,719	1,075	65	20	4	11	56	32	12			0.44	82
30R-7, 29	588	23,179	5,337	4,658	998	54	26	10	10	43	40	17	15.97	26	0.55	77
30R-7, 35	588	33,363	6,366	5,471	1,258	59	24	8	8	48	36	16	15.87	19	0.95	55
30R-7, 47	588	34,599	6,879	5,817	896	63	26	7	4	47	37	16	15.95	25	0.58	75
31R-1, 17	588	36,215	10,099	8,097	958	54	32	10	4	39	44	17	15.99	27	0.60	75

Table T1 (continued).

Core, section, interval (cm)	Depth (mbsf)	XRD peak area (total counts)				Relative mineral abundance: SVD factor (wt%)				Relative mineral abundance: Biscaye factor (area%)			I/S mixed-layer clay			
		Smectite	Illite	Chlorite (+kaolinite)	Quartz	Smectite	Illite	Chlorite (+kaolinite)	Quartz	Smectite	Illite	Chlorite (+kaolinite)	I(002)/S(003) (Å)	Illite in I/S (%)*	I-saddle: I-peak	Expandability (%)†
31R-2, 57	590	41,801	2,525	2,504	1,097	87	9	0	4	73	18	9			0.37	85
31R-CC, 8	591	29,966	3,551	3,497	1,012	70	18	5	8	59	28	14	15.81	11	0.49	80
32R-1, 64	598	10,836	2,731	3,517	735	44	24	17	14	38	38	24	16.14	42	0.78	67
33R-1, 11	608	53,240	12,144	15,994	1,295	53	27	17	4	40	36	24	15.82	13	0.29	90
33R-1, 88	608	7,690	2,633	3,548	693	37	26	20	16	30	42	28			0.88	62
33R-2, 72	610	9,318	4,910	5,909	902	32	31	22	15	23	48	29	15.86	18	0.83	65
34R-CC, 13	617	10,358	4,786	6,498	1,218	33	28	22	17	24	45	31	16.1	39	0.74	69
35R-2, 67	628	35,529	4,279	4,111	800	76	18	3	2	58	28	14	15.83	14	0.52	78
35R-3, 13	628	7,843	3,996	4,762	1,147	32	28	20	19	24	48	29			0.77	68
36R-1, 24	637	12,675	4,523	3,752	663	44	32	13	10	33	47	20	15.92	23	0.76	68
36R-1, 112	637	12,301	4,199	5,329	1,216	38	26	19	17	31	42	27	15.94	24	0.75	68
37R-2, 82	647	25,545	7,328	8,542	1,346	45	27	17	11	36	41	24			0.61	74
37R-3, 34	648	16,053	6,434	5,735	1,024	40	32	15	12	30	48	22			0.74	69
38R-CC, 22	656	2,896	1,424	2,026	1,236	30	21	19	30	23	45	32			0.86	63
39R-1, 96	666	28,362	3,561	3,152	1,239	65	18	5	11	58	29	13			0.47	80
40R-1, 115	676	36,297	4,678	2,862	1,085	75	19	0	6	60	31	9			0.37	85
41R-1, 129	686	28,804	3,849	2,768	775	74	20	1	4	58	31	11	15.91	22	0.53	78
41R-2, 97	687	29,405	4,197	3,120	1,002	69	21	3	7	56	32	12			0.40	84
42R-1, 116	695	22,181	2,681	1,624	1,023	68	18	2	12	61	30	9			0.52	78
43R-1, 3	704	28,265	2,964	2,175	1,210	70	16	2	11	64	27	10	15.8	10	0.51	79
44R-1, 37	714	37,015	4,873	3,723	1,162	72	19	3	6	58	30	12			0.51	79
44R-2, 70	716	24,403	2,930	2,813	1,143	64	17	6	12	58	28	13			0.54	77
45R-2, 87	725	10,884	1,901	1,786	1,088	48	20	11	22	49	34	16			0.67	72
46R-1, 18	733	26,459	3,506	2,744	956	69	19	4	8	58	31	12			0.53	78
46R-1, 120	734	24,383	3,251	2,315	1,102	66	19	4	12	58	31	11	15.82	13	0.52	78
46R-2, 122	735	34,044	3,262	3,515	1,869	64	15	6	15	63	24	13			0.42	83
46R-3, 9	736	40,710	5,574	3,683	1,394	71	20	2	8	58	32	10			0.49	80
47R-3, 101	746	20,593	3,667	3,642	1,243	54	21	10	15	48	34	17	15.96	25	0.62	74
		Average Lower Shikoku turbidite facies:				49	28	13	11	38	42	20				
47R-5, 97	749	22,544	3,549	2,949	1,115	60	21	7	12	53	33	14			0.55	77
48R-4, 108	757	4,998	3,344	2,225	1,655	31	26	15	28	22	59	19	15.95	25	0.80	66
48R-4, 117	757	25,397	4,308	3,857	1,085	60	22	8	10	50	34	15			0.56	76
48R-6, 113	760	23,797	4,573	4,604	690	60	25	10	5	46	36	18			0.65	73
48R-7, 7	761	23,916	3,203	2,086	509	78	21	0	1	58	31	10			0.48	80
49R-1, 61	762	20,587	7,829	4,843	2,048	41	30	11	18	33	51	16			0.44	82
49R-2, 63	763	45,916	3,568	2,185	1,590	80	12	0	8	71	22	7			0.45	81
49R-2, 148	764	9,727	1,798	1,089	689	54	22	6	17	51	38	11			0.65	73
49R-3, 115	765	32,483	3,168	1,366	1,138	77	15	0	8	68	26	6			0.50	79
49R-4, 20	766	29,032	2,073	430	643	90	10	0	1	76	22	2			0.57	76
49R-4, 29	766	34,819	3,330	658	771	85	14	0	1	70	27	3	15.88	20	0.47	80
49R-5, 72	768	12,949	2,051	1,038	598	65	22	2	12	56	35	9	15.81	11	0.67	72
50R-3, 0	774	18,173	3,954	3,402	765	55	26	9	9	45	39	17	15.91	22	0.63	73
50R-3, 32	774	9,952	2,086	1,535	502	56	25	8	12	47	39	14			0.74	69
50R-3, 39	774	12,217	2,856	2,458	829	49	25	11	15	43	40	17	15.9	21	0.67	72
51R-1, 15	781	8,394	1,121	447	214	77	20	0	3	61	33	6			0.71	70
51R-2, 23	782	13,471	2,190	1,130	463	69	23	1	7	55	36	9			0.65	73

Table T1 (continued).

Core, section, interval (cm)	Depth (mbsf)	XRD peak area (total counts)				Relative mineral abundance: SVD factor (wt%)				Relative mineral abundance: Biscaye factor (area%)			I/S mixed-layer clay			
		Smectite	Illite	Chlorite (+kaolinite)	Quartz	Smectite	Illite	Chlorite (+kaolinite)	Quartz	Smectite	Illite	Chlorite (+kaolinite)	I(002)/S(003) (Å)	Illite in I/S (%)*	I-saddle: I-peak	Expandability (%)†
51R-2, 102	783	17,865	3,508	1,963	682	63	26	3	8	50	39	11	15.91	22	0.63	73
51R-2, 109	783	5,162	843	484	677	47	18	9	26	54	35	10			0.78	67
51R-2, 109	783	7,271	1,368	677	550	54	22	5	18	52	39	10			0.78	67
51R-2, 134	783	13,977	3,501	1,677	1,052	51	26	6	17	45	45	11	15.95	25	0.66	72
52R-2, 18	792	26,519	1,846	1,271	699	86	10	0	4	73	20	7	15.9	21	0.52	78
52R-2, 18	792	26,519	1,841	1,358	764	84	10	0	5	72	20	7	15.93	23	0.52	78
52R-2, 56	792	24,739	1,713	1,579	340	91	9	0	0	71	20	9	15.8	10	0.55	77
52R-3, 28	794	19,617	2,613	359	621	75	19	0	6	64	34	2	15.91	22	0.66	72
52R-3, 49	794	16,719	3,135	1,350	789	62	24	2	12	52	39	8			0.62	74
53R-2, 57	802	22,579	5,754	697	901	61	31	0	8	48	49	3	15.82	13	0.58	75
53R-3, 119	804	19,252	4,313	2,597	1,468	51	24	8	17	46	41	12	15.87	19	0.61	74
54R-1, 128	811	15,934	1,289	733	457	83	12	0	5	71	23	6	15.96	25	0.65	73
54R-2, 48	811	23,684	4,149	1,107	671	71	25	0	4	56	39	5	15.96	25	0.61	74
54R-3, 70	813	14,601	2,677	1,340	1,121	54	22	6	19	52	38	10			0.63	73
54R-5, 55	816	17,012	2,240	1,416	1,281	57	18	6	19	59	31	10	15.83	14	0.61	74
55R-1, 92	820	8,128	6,195	7,347	793	27	35	24	13	17	52	31	16.03	30	0.83	65
55R-1, 109	820	24,974	5,563	2,553	1,091	60	27	3	10	48	43	10			0.60	75
55R-1, 116	820	24,985	3,620	1,945	1,132	66	20	2	12	58	33	9	15.93	23	0.54	77
55R-1, 120	820	20,782	4,221	2,137	1,057	59	25	4	12	50	40	10			0.63	73
56R-1, 120	830	15,759	2,189	842	673	69	20	0	11	60	33	6	15.87	19	0.69	71
56R-2, 48	831	18,013	4,956	2,580	839	54	30	5	10	42	46	12	15.81	11	0.60	75
56R-2, 74	831	62,895	4,788	1,872	956	90	10	0	0	73	22	4			0.45	81
Average volcaniclastic-rich facies:						64	21	4	10	54	35	10				

Notes: SVD (singular value decomposition) normalization factors from **Underwood et al.** (this volume). Peak area weighting factors from Biscaye (1965). * = Calculation follows Reynolds and Hower (1970) with peak position corrected to quartz (100). † = Calculation follows Rettke (1981) assuming 3:1 ratio of discrete illite to illite (I)/smectite (S) mixed-layer clay. XRD = X-ray diffraction.

Table T2. Results of X-ray diffraction analyses before and after boiling clay in HCl.

Core, section, interval (cm)	Treatment	Depth (mbsf)	Facies	Measured peak area		Scaled peak area*		Area ratio†
				Quartz	Chlorite + Kaolinite	Quartz	Chlorite + Kaolinite	
190-1173A-								
72X-1, 126	Untreated	678.00	LSB	970	7945	970	7945	0.12
72X-1, 126	+ HCl			1137	1097	970	936	
73X-1, 117	Untreated	687.50	LSB	1379	3531	1379	3531	0.00
73X-1, 117	+ HCl			1195	0	1379	0	
190-1177A-								
32R-1, 64	Untreated	598.44	LSBt	752	3596	752	3596	0.28
32R-1, 64	+ HCl			1166	1576	752	1016	
46R-1, 120	Untreated	733.70	LSBt	1245	2482	1245	2482	0.60
46R-1, 120	+ HCl			1482	1775	1245	1491	
55R-1, 120	Untreated	830.00	Volc-rich	1049	2198	1049	2198	0.10
55R-1, 120	+ HCl			720	144	1049	210	

Notes: LSB = lower Shikoku Basin, LSBt = lower Shikoku Basin turbidite, volc-rich = volcaniclastic rich. * = Peak area scaled by factors that set quartz (100) before HCl to quartz (100) after HCl. † = Ratio of peak area for scaled treated sample:peak area for untreated sample.

Table T3. Paleomagnetic and nannofossil ages used in kinetic model of smectite-to-illite reaction.

Site	Depth interval (mbsf)	Age at base (Ma)	Burial rate (m/m.y.)
190-			
1173	0–160	0.8	205.1
	160–390	4.0	71.4
	390–590	12.4	23.8
	590–650	13.6	50.0
	650–720	14.1	140.0
1174	0–540	0.8	692.3
	540–690	2.6	83.3
	690–950	10.9	31.3
	950–1110	13.4	64.0
1177	0–310	2.0	159.0
	310–370	2.6	95.1
	370–440	6.6	17.6
	440–750	15.6	34.3
	750–800	18.6	16.7
131-			
808	0–660	0.8	795.2
	660–790	1.9	122.6
	790–900	4.1	49.8
	900–1000	6.7	38.5
	1000–1090	11.1	20.5
	1090–1220	13.5	54.2

Note: Site 1173 ages from Shipboard Scientific Party (2001c), Site 1174 ages from Shipboard Scientific Party (2001d), Site 1177 ages from Shipboard Scientific Party (2001e), Site 808 ages from Olafsson (1993).